Antisense oligonucleotide allele-specific targeting of EFEMP1 in a patient-derived model of Doyne honeycomb retinal dystrophy

Farah. O. Rezek,[1,3] Beatriz Sanchez-Pintado,[1,3] Emily R. Eden,[1] Nancy Aychoua,[2] Andrew R. Webster,[1,2] Amanda-Jayne F. Carr,[1] Michel Michaelides,[1,2] Michael E. Cheetham,[1] Jacqueline van der Spuy[1]

[1]UCL Institute of Ophthalmology, University College London, London EC1V 9EL, UK

[2]Moorfields Eye Hospital NHS Foundation Trust, London, United Kingdom

[3]These authors contributed equally to this work

Correspondence should be addressed to: Jacqueline van der Spuy, University College London Institute of Ophthalmology. University College London, 11 – 43 Bath Street, London, EC1V 9EL, UK. **Telephone:** +44 02076086910. **E-mail:** j.spuy@ucl.ac.uk

Short title: EFEMP1 ASO

ABSTRACT

Doyne honeycomb retinal dystrophy is an incurable juvenile macular dystrophy that leads to visual impairment by early to mid-adulthood. It is an autosomal dominant disorder caused by a c.1033C>T, p.Arg(345Trp) variant in *EFEMP1*, and is characterised by the early onset extracellular deposition of drusen between the retinal pigment epithelium basement membrane and underlying layers of Bruch's membrane. In this study, we developed an antisense oligonucleotide approach to target *EFEMP1*. We reprogrammed patient-derived renal epithelial cells to induced pluripotent stem cells followed by directed differentiation to retinal pigment epithelium and compared the phenotype to gene-corrected and *EFEMP1* knockout patient-derived retinal pigment epithelium. In the patient-derived disease model, remodelling of the extracellular matrix occurred with progressive accumulation of extracellular deposits containing the drusen-associated proteins apolipoprotein E and collagen IV, in addition to EFEMP1. Moreover, the intracellular accumulation of neutral lipids was evident. We developed an allele-specific antisense oligonucleotide which specifically and effectively promoted the clearance of the *EFEMP1* c.1033C>T transcript in the patient-derived disease model following assisted or gymnotic delivery. In this disease model, gymnotic delivery led to a decrease in extracellular deposits and cleared the intracellular accumulation of lipids, even after the onset of this disease phenotype, suggesting this could be a practical and effective therapeutic approach.

INTRODUCTION

Doyne honeycomb retinal dystrophy (DHRD) is a progressive and incurable juvenile macular dystrophy that is characterised by the early onset radial deposition of peripapillary and macular drusen that merge over time in a 'honeycomb' pattern.[1,2]

45 The lipoproteinaceous drusen are deposited extracellularly between the retinal
46 pigment epithelium (RPE) basement membrane and underlying layers of Bruch's
47 membrane. Though the onset of visual symptoms varies, DHRD typically leads to
48 visual impairment in early to mid-adulthood. However, extensive drusen can be
49 present as early as the second decade of life.[1,2] Early visual symptoms include
50 decreased visual acuity, photophobia, metamorphopsia, dyschromatopsia and relative
51 scotomas that progress to atrophy of the retinal pigment epithelium (RPE) leading to
52 central visual loss. A worse prognosis is associated with choroidal neovascularisation
53 (CNV).[3]
54
55 DHRD is an autosomal dominant disorder caused by the c.1033C>T, p.(Arg345Trp)
56 variant in the *epidermal growth factor (EGF)-containing fibulin-like extracellular matrix*
57 *protein 1* (*EFEMP1*) gene.[4] The EFEMP1, or fibulin 3 (F3), protein is an extracellular
58 glycoprotein that is synthesised by the RPE and secreted into the collagen IV-rich RPE
59 basement membrane where it contributes to the structural integrity of the extracellular
60 matrix (ECM). The Arg345Trp substitution is in the final Ca^{2+} binding EGF domain of
61 EFEMP1, which alters disulphide bond formation and the structural integrity of the
62 protein, resulting in increased stability and accumulation of the mutant protein in the
63 ECM.[5-8] Extracellular accumulation of EFEMP1 Arg345Trp also causes increased
64 expression of its binding partner, tissue inhibitor of metalloproteinase 3 (TIMP3),
65 resulting in reduced matrix metalloproteinases (MMP) activity, such as MMP2 and
66 MMP9, and creating an imbalance that results in the accumulation of ECM
67 aggregates.[9,10] The remodelling process triggers an interplay that increases levels of
68 complement component 3 (C3) and complement factor B (CFB) that exacerbates the
69 ECM remodelling and sub-RPE deposition.[11-13] Moreover, EFEMP1 Arg345Trp has

70 been shown to exert a hyper-inhibitory effect on epidermal growth factor receptor
71 (EGFR) signalling, potentially through the deactivation of the PI3K/AKT pathway. This
72 disruption leads to reduced expression of carboxylesterase 1 (CES1), impairing
73 cholesterol efflux and resulting in abnormal lipid accumulation within RPE cells and
74 the basement membrane.[14] These pathological changes collectively disrupt the
75 structural and functional integrity of the RPE basement membrane leading to the
76 deposition of drusen containing components such as apolipoprotein E (APOE), C3
77 and TIMP3. Increased accumulation of sub-RPE basal deposits rich in lipids and
78 proteins, including APOE, TIMP3 and EFEMP1, has been reported in a patient-derived
79 DHRD RPE disease model.[13]
80
81 Patients that harbour biallelic loss-of-function *EFEMP1* variants develop a pronounced
82 connective tissue disease characterised by multiple and recurrent abdominal and
83 thoracic herniae, myopia, hypermobile joints, scoliosis, and thin translucent skin,
84 however macular dystrophy is absent in these patients.[15] Moreover, macular
85 dystrophy is absent in *Efemp1* knockout mice and the knockout of *Efemp1* has been
86 shown to be protective against the development of sub-RPE deposits.[16,17] These data
87 support an EFEMP1 Arg345Trp toxic gain-of-function and the absence of
88 haploinsufficiency in DHRD.
89
90 Therefore, in this study, we designed an allele-specific antisense oligonucleotide
91 (ASO) therapy to induce the knockdown of variant *EFEMP1* expression in a patient-
92 derived disease model of DHRD. We reprogrammed patient renal epithelial cells to
93 induced pluripotent stem cells (iPSCs) followed by directed differentiation to RPE
94 (iRPE). Our patient iRPE model faithfully recapitulated the disease phenotype,

95 including the accumulation of lipids, remodelling of the ECM and the sub-RPE
96 deposition of drusen-associated components. The treatment of patient-derived iRPE
97 with therapeutic ASO resulted in allele-specific targeting of *EFEMP1* Arg345Trp and
98 efficient resolution of pathogenic changes, even after the onset of the disease
99 phenotype *in vitro*.
100
101 RESULTS
102 **DHRD patient clinical phenotype**
103 Renal epithelial cells were purified from urine of a 60-year-old male patient clinically
104 diagnosed with DHRD and confirmed to harbour the autosomal dominant *EFEMP1*
105 variant c.1033C>T, p.Arg(345Trp). The patient was first diagnosed with DHRD in his
106 early twenties, presymptomatically, following retinal examination due to the family
107 history. Ultra-widefield fundus images (Optos scanning laser ophthalmoscope) and
108 autofluorescence images showed hyperautoflourescent deposits at the macula, some
109 with a radial configuration, with deposit directly adjacent to the optic disc (Figure S1).
110 Heidelberg Spectralis optical coherence tomography (OCT) images showed
111 extensive, hyperreflective deposit underlying the neurosensory retina, greater at the
112 left macula than the right (Figure S1).
113 **Correction of *EFEMP1* c.1033C>T and *EFEMP1* knockout in patient iPSC**
114 The DHRD patient renal epithelial cells were reprogrammed to induced pluripotent
115 stem cells (iPSCs) as described previously.[18,19] CRISPR-Cas9 homology directed
116 repair (HDR) using *in vitro* assembled *EFEMP1* crRNA/tracrRNA-Cas9 ribonucleotide
117 protein (RNP) together with a single stranded oligonucleotide (ssODN) repair template
118 was used to correct the c.1033C>T, p.Arg(345Trp) variant in the patient iPSC line
119 thereby generating an isogenic control (Figure S2A). In addition, the ssODN repair

120 template introduced a heterozygous synonymous change in the protospacer adjacent
121 motif (PAM). CRIPSR-Cas9 non homologous end joining (NHEJ) targeting *EFEMP1*
122 exon 5 introduced a homozygous insertion of a single nucleotide (G) inducing a frame
123 shift and premature translation termination of the *EFEMP1* transcript (c.215_216insG,
124 p.Lys73GlufsX81) (Figure S2B). crRNA and ssODN sequences are listed in
125 Supplemental Tables 1 and 2 (Table S1, Table S2). No off-target editing was observed
126 in the isogenic lines at the top 10 predicted off-target genomic loci (Table S3). iPSC
127 cultures from the DHRD patient iPSC (R345W), isogenic repaired iPSC (ISOCON)
128 and isogenic knockout (ISOKO) lines uniformly expressed pluripotency markers
129 (*OCT4*, *NANOG*, *TRA1-181*, and *SSEA4*) (Figure S2C).

130 **Phenotypic characteristics of patient iPSC-iRPE (iRPE)**

131 iPSC lines were differentiated to RPE by the method described in Regent *et al.*
132 (2019).[20] Light microscopy images taken of the isogenic control (ISOCON) and
133 R345W patient line at day 60 of RPE differentiation (Figure 1A), demonstrated a typical
134 RPE cobblestone morphology, with pronounced cell borders. The ISOCON iRPE
135 formed a homogenous monolayer, while the R345W iRPE displayed a more
136 heterogenous morphology. Immunofluorescence (IF) analysis of both iRPE lines
137 demonstrated clear expression of the tight junction protein ZO-1, which localized to
138 the cell-cell borders in a continuous, hexagonal pattern consistent with the formation
139 of an epithelial monolayer with tight junctions (Figure 1A). PMEL, a marker of
140 melanosome biogenesis, was also detected in both lines, appearing as intracellular
141 puncta indicative of developing pigment organelles (Figure 1A). These data confirm
142 the expression of key RPE markers associated with epithelial identity and early
143 melanosome formation. Western blot analyses of both lines demonstrated robust

144 expression of the RPE characteristic markers ZO-1, Ezrin and MERTK at day 110 of
145 differentiation (Figure 1B).
146 At day 80 and day 96, immunostaining of the ISOCON and R345W iRPE revealed
147 phenotypic differences in the pattern and localisation of key RPE markers (Figure 1C).
148 The R345W iRPE displayed a markedly patchy and heterogenous PMEL distribution,
149 with areas of diminished signal interspersed among irregularly distributed PMEL-
150 positive regions, potentially indicating a delay in iRPE maturity relative to the ISOCON
151 iRPE. MERTK immunostaining was primarily localised to the plasma membrane as
152 expected and illustrated the differences in cell morphology between the ISOCON and
153 R345W iRPE at both timepoints, with a less organised and more heterogeneous cell
154 population apparent in the R345W line, that deteriorated between the day 80 and day
155 96 timepoints. Immunostaining of collagen IV (COL4), a marker of the basement
156 membrane, exhibited an evenly distributed and homogenous pattern, reflecting a well-
157 organised basement membrane in ISOCON iRPE. Conversely, the COL4
158 immunolocalisation in the R345W iRPE, exhibited an uneven pattern, with bright
159 accumulations, reflecting a disrupted basement membrane. Similarly, Ezrin
160 immunolocalisation, which marks the apical microvilli, was uniform in the ISOCON line
161 but appeared patchy and irregular in the R345W line. APOE deposits were observed
162 in both the ISOCON and R345W iRPE at the day 80 and 96 timepoints; however,
163 deposits were larger and more extensively distributed in the R345W line, suggesting
164 that this substitution leads to increased APOE accumulation, a major component of
165 drusen formation. These results collectively showed that both the ISOCON and
166 R345W iPSC lines could form RPE, as evidenced by the expression of hallmark RPE
167 markers. However, the presence of the R345W variant results in phenotypic
168 alterations, suggesting that while fundamental RPE differentiation is preserved, the

169 variant disrupts the structural organisation of the extracellular matrix components,
170 potentially compromising RPE function and contributing to disease pathology.

171 **Apicobasal characteristics of patient iPSC-iRPE (iRPE)**

172 To characterise the iRPE and confirm their apicobasal polarity, day 98 vertically
173 embedded cross sections were immunostained for RPE markers (Figure 2). The
174 ISOCON iRPE formed a well-organised, uniform monolayer. Ezrin was appropriately
175 localised to the apical surface, with COL4 immunolocalisation marking a continuous
176 and uniform basal layer (Figure 2A). In contrast, the R345W iRPE displayed a
177 disorganised phenotype, with a dysmorphic basal membrane and the cells failing to
178 form a uniform monolayer. COL4 immunolocalisation revealed a disrupted and
179 thickened basement membrane, indicating abnormalities in structural integrity (Figure
180 2A). Distribution of PMEL localisation was comparable between the ISOCON and
181 R345W iRPE, although ZO-1 localisation at cell-cell junctions appeared more
182 fragmented and discontinuous in the R345W line relative to the control, potentially
183 indicating a disruption of tight-junctions in these cells (Figure 2B). IF for EFEMP1
184 (fibulin 3 (F3)) was conducted in ISOCON, R345W and ISOKO iRPE (Figure 2C).
185 ISOCON iRPE exhibited a clustered distribution of F3 across the basal layer, with the
186 R345W iRPE also demonstrating a similar pattern but with the appearance and
187 accumulation of more filamentous-shaped F3. Immunolocalisation of F3 in the ISOKO
188 iRPE demonstrated both that *EFEMP1* expression was successfully knocked out of
189 this cell line and that the antibody used was specific to F3, as no signal was
190 observed. Moreover, COL4 immunolocalisation in the ISOKO iRPE was similar to that
191 in the ISOCON iRPE, demarcating a continuous and well-organised basement
192 membrane (Figure 2C).

193 The ultrastructure of ISOCON and R345W iRPE was examined by TEM at day 158 of
194 differentiation (Figure 2D). Both ISOCON and R345W iRPE demonstrated a typical
195 polarised RPE morphology with basally located nuclei, numerous elongated microvilli
196 extending from the apical surface and cytoplasm rich in melanin granules
197 concentrated apically (Figure 2D, upper panel). However, basal deposits were visible
198 between the basement membrane (blue outline) and the underlying transwell
199 membrane in patient-derived iRPE cells (Figure 2D, upper panel). Additionally, both
200 ISOCON and R345W iRPE contained abundant mitochondria. However, altered
201 morphology of mitochondria (false-coloured green), which were sometimes elongated,
202 were observed in the R345W iRPE with the cristae often appearing to be orientated
203 longitudinally (Figure 2D, lower panel), raising the possibility of mitochondrial
204 dysfunction as a feature of the disease pathology.

205 ***In vitro* screen of antisense oligonucleotides targeting *EFEMP1* c.1033C>T**

206 Four 18-mer ASO (ASO1-4) spanning the c.1033C>T variation in *EFEMP1* (Table S4)
207 were designed to induce RNase H1-mediated degradation of the *EFEMP1* target
208 mRNA and analysed *in silico* as described previously.[21] The thermodynamic binding
209 stability of each ASO sequence was analysed *in silico* using a 124 bp sequence
210 comprising exon 10 of R345W *EFEMP1* as target RNA (RNAstructure, University of
211 Rochester) to determine the difference in free energy of the target sequence alone in
212 comparison to the ASO bound target sequence, as shown for ASO1 (Figure 3A). This
213 analysis confirmed the stable binding of all ASO to the target sequence. An *in vitro*
214 screen of ASO1-4 in HEK293T cells was conducted to determine their ability to knock
215 down *EFEMP1* (Figure 3B-E). HEK293T cells co-transfected with R345W *EFEMP1*-
216 mScarlet and WT *EFEMP1*-FLAG were treated with control ASO (CTRL) (50 nM) or
217 increasing concentrations (25 nM, 50 nM, 100 nM, 200 nM) of ASO1, 2, 3 or 4.

218 Quantitation of R345W *EFEMP1* (Figure 3B), WT *EFEMP1* (Figure 3C) and total
219 *EFEMP1* (Figure 3D) transcripts by qPCR showed a reduction in all *EFEMP1* levels
220 (R345W, WT, TOTAL) compared to the CTRL ASO and untreated cells (plasmids only)
221 only with ASO1 (Figure 3). Reduced levels of *EFEMP1* (R345W, WT, TOTAL) with
222 ASO2 were evident only at the highest and lowest concentrations. No reduction of
223 *EFEMP1* R345W, WT or TOTAL transcript levels was evident with ASO3 or with
224 ASO4. No expression of *EFEMP1* was detected in cells that were mock transfected
225 (UT). Four derivatives of the best-preforming ASO1 (ASO1.1-1.4) (Table S4) were
226 tested *in vitro* in HEK293T cells (Figure 3E). Levels of *EFEMP1* (TOTAL, R345W, WT)
227 were measured by qPCR. All ASO, except for ASO1.2, showed a concentration-
228 dependent decline in *EFEMP1* (TOTAL, R345W, WT) transcript levels compared to
229 the untreated (plasmid only) and control ASO (CTRL) conditions, and the highest level
230 of *EFEMP1* reduction was achieved with 200 nM ASO1.1. Whilst ASO1.2 could
231 effectively reduce *EFEMP1* levels at all concentrations tested, the ASO1.2-mediated
232 reduction in *EFEMP1* levels was not concentration-dependent. All ASO (1.1-1.4)
233 mediated a greater reduction in R345W *EFEMP1* compared to WT *EFEMP1* (Figure
234 3E).

235 **Allele-specific *EFEMP1* targeting following ASO transient transfection of iRPE**

236 To assess the efficacy of ASO treatment in the downregulation of *EFEMP1* transcript
237 expression, ASOs 1.1-1.4 were transiently transfected into R345W EFEMP1 patient-
238 derived iRPE at a dose of 200 nm at day 72 of differentiation. Transfection of the 6-
239 FAM-labelled ASO1.1 into the R345W iRPE, resulted in strong intracellular
240 fluorescence (Figure 4A). Experimental cell samples were lysed 48 hours post-
241 transfection for transcript-level analyses. qPCR analysis demonstrated a significant
242 30-40% reduction of total *EFEMP1* transcript levels in therapeutic ASO-treated

243 conditions, relative to transfection reagent only (NT) and control ASO treated
244 conditions (CTRL), suggesting an effective downregulation of *EFEMP1* expression by
245 the designed ASOs (Figure 4B).
246 To explore allele-specificity, Sanger sequencing of cDNA amplicons spanning the
247 c.1033C>T variant revealed preferential downregulation of the R345W transcript
248 (Figure 4C). Electropherogram traces from therapeutic ASO-treated samples
249 demonstrated marked reduction in the peak corresponding to the variant 'T' base
250 relative to NT and CTRL conditions, providing semi-quantitative confirmation of allele-
251 specificity of the ASOs.
252 Targeted next generation sequencing (NGS) was conducted using primers (Table S5)
253 producing an amplicon covering the c.1033C>T locus of *EFEMP1* to enable
254 quantitation of the allelic discrimination of the ASOs (Figure 4D). A baseline of allelic
255 expression in the DHRD patient-derived samples was obtained to observe the
256 possibility of *EFEMP1* allele skewing (Figure 4D). Amplicon quantitation of gDNA from
257 patient-derived renal epithelial cells confirmed the expected 50:50 ratio between the
258 WT and R345W alleles of *EFEMP1*, confirming equal copy number. cDNA prepared
259 from renal epithelial cells of the patient also demonstrated a 50:50 ratio between the
260 WT and R345W alleles of *EFEMP1*, indicating that in this cell type, both alleles of
261 *EFEMP1* are equally expressed. However, basal expression levels of the cDNA
262 prepared from differentiated iRPE in the NT and CTRL ASO treated conditions
263 revealed a 55:45 WT:R345W allelic expression split, indicating that the WT allele is
264 expressed slightly higher than the R345W allele in differentiated iRPE. Following
265 therapeutic ASO treatment, a clear reduction in R345W allele expression was
266 observed for all ASOs, corroborating the Sanger sequencing data (Figure 4C).
267 Therapeutic ASO treatment through transient transfection resulted in the WT allele

268 constituting 84.4-88.3% of total allelic expression, and the R345W allele constituting
269 11.7-15.6% of total allelic expression (Figure 4D).
270 Integrated analysis of the qPCR (Figure 4B) and NGS (Figure 4D) was performed to
271 gain an understanding of how the ASO treatments affect the expression of the
272 *EFEMP1* WT and R345W alleles relative to total *EFEMP1* transcript expression
273 (Figure 4E). The percentage of allelic expression was calculated in comparison to total
274 levels of *EFEMP1* transcript (Figure 4B) before normalisation of the data to the NT
275 control condition for the respective data group (WT or R345W allele) (Figure 4D). No
276 significant differences between the control (NT and CTRL ASO) and therapeutic ASO
277 treatment conditions were observed for the expression of the WT allele, with significant
278 reductions in the R345W allele expression clearly observed following therapeutic ASO
279 treatment. These results thus demonstrated consistent R345W allele-specific
280 downregulation following treatment with the therapeutic ASOs. Based on these data,
281 ASO1.1 was taken forward for the rest of the ASO treatments, due to its high
282 reproducibility in reducing R345W *EFEMP1* allele expression and its ideal length (16-
283 mer).
284 **Allele-specific *EFEMP1* targeting following ASO gymnosis of iRPE**
285 Gymnotic (unassisted) delivery of ASO1.1 at day 60 of differentiation was carried out
286 to evaluate ASO efficacy in a setting that more closely recapitulates physiological
287 uptake mechanisms (Figure 5). Fluorescence microscopy of gymnotically delivered 6-
288 FAM-conjugated ASO1.1 (1 μM) showed efficient uptake across the R345W iRPE
289 population following a 7-day treatment (Figure 5A). The ASO was demonstrated to
290 robustly accumulate in the nucleus, with additional punctate localisation in the
291 cytoplasm. This distribution is consistent with the known subcellular activity of RNase
292 H1, which is present in both the nucleus and cytoplasm.[22] While the ASO is designed

293 to target mature mRNA, their nuclear localisation suggests potential additional
294 engagement with pre-mRNA targets. RNase H-mediated cleavage of the target
295 transcript can occur in both subcellular compartments, with cytoplasmic ASO signal
296 potentially indicating interactions with mature transcripts or transient endosomal
297 retention. Thus, ASO localisation in both of these compartments indicates enhanced
298 likelihood of effective target knockdown following gymnotic uptake.
299 R345W iRPE underwent a 7-day treatment with ASO1.1 at the doses 0.5 µM, 1 µM, 5
300 µM and 10 µM, and *EFEMP1* gene expression was analysed by qPCR (Figure 5B).
301 Therapeutic ASO treatments at each of the doses led to a significant downregulation
302 of total *EFEMP1* expression relative to the NT and CTRL ASO treatment conditions.
303 However, no clear dose-dependent response was observed between therapeutic ASO
304 treatments. The magnitude of *EFEMP1* knockdown remained comparable between
305 the lowest and highest ASO doses tested. This plateau in response indicates that
306 maximal target suppression could be achieved at or below the lowest tested
307 concentration.
308 Next, targeted NGS was employed to evaluate the allelic discrimination of gymnotically
309 delivered ASOs (Figure 5C). Baseline allelic expression in iRPE for the DHRD patient
310 included in this study was confirmed at a 55:45 WT:R345W allelic split, as observed
311 in the NT and CTRL ASO conditions. Again, there was no dose-dependent response
312 following ASO1.1 treatment at the doses 0.5 µM, 1 µM, 5 µM and 10 µM as all doses
313 led to the WT allele constituting 73-78% and the mutant allele constituting 22-27% of
314 total *EFEMP1* expression.
315 Integrated analysis of the qPCR (Figure 5B) and targeted NGS (Figure 5C) data was
316 carried out to explore the efficacy of ASO1.1 in its allele-specific downregulation of
317 *EFEMP1*. The percentage of allelic expression was calculated in comparison to total

318 levels of *EFEMP1* transcript (Figure 5B) with normalisation of the data to the NT
319 control condition for the respective data group (WT or R345W allele) (Figure 5D).
320 Similar to the qPCR and NGS data collation carried out for the transient transfection
321 (Figure 4D), no significant differences between the controls (NT and CTRL ASO) and
322 therapeutic ASO treatment conditions were observed for WT allele expression,
323 whereas significant reductions in mutant *EFEMP1* was clearly observed. Overall, this
324 confirmed consistent *EFEMP1* R345W allele-specific downregulation via ASO1.1
325 gymnosis.

326 **Rescue of patient iRPE phenotype following ASO gymnosis**

327 We next examined the phenotype of patient iRPE following gymnotic treatment with
328 the therapeutic ASO1.1 (Figure 6). To assess the impact of ASO gymnosis on APOE,
329 whole-mount iRPE samples following a 1-week treatment starting from day 60 of
330 differentiation were immunolabelled for APOE (Figure 6A). APOE has been shown to
331 accumulate in sub-RPE deposits and contribute to drusen formation, hallmarks of
332 DHRD. IF analysis revealed low APOE signal for both the ISOCON and ISOKO iRPE.
333 In contrast, NT R345W iRPE exhibited a marked increase in APOE fluorescence,
334 consistent with the DHRD disease phenotype. 1-week gymnosis of ASO1.1 at a dose
335 of 1 μM resulted in a substantial reduction in APOE fluorescence, as illustrated in the
336 representative images and by quantification of total fluorescence intensity (Figure 6A
337 and B). Quantitative analysis confirmed a significant elevation of APOE levels in the
338 R345W NT condition relative to ISOCON and ISOKO iRPE. There was no difference
339 in the levels of APOE quantified in the ISOCON and ISOKO iRPE. APOE levels in the
340 ASO-treated R345W iRPE displayed significantly reduced APOE fluorescence relative
341 to the NT condition, although expression remained modestly higher than in the
342 ISOCON and ISOKO condition, following the 1-week treatment. These findings

343 indicate that suppression of R345W *EFEMP1* via gymnotically delivered ASO
344 mitigates downstream APOE accumulation, implicating a functional relationship
345 between *EFEMP1*-driven pathology and APOE accumulation in this iRPE model.
346 Next, the distribution of APOE and lipid accumulation in vertically embedded iRPE
347 cross sections was assessed following a 2-week gymnotic ASO1.1 treatment, initiated
348 on day 84 of differentiation, at concentrations of 1 μM and 5 μM (Figure 6C). Sections
349 were stained with BODIPY to visualise neutral lipid content and co-labelled for APOE.
350 ISOCON iRPE exhibited minimal BODIPY and APOE immunoreactivity, whereas
351 patient-derived iRPE treated with CTRL ASO displayed elevated fluorescence signals
352 for both markers. In contrast, ASO1.1-treated iRPE showed a pronounced reduction
353 in BODIPY and APOE fluorescence intensity at both 1 μM and 5 μM doses, indicating
354 that gymnotic ASO1.1 administration effectively decreases APOE expression and lipid
355 accumulation in patient-derived DHRD iRPE within two weeks.
356 To further investigate the robustness of ASO1.1 effects and its potential impact on
357 ECM organisation, a 2-month gymnotic treatment was conducted on patient-derived
358 iRPE (Figure 7). ISOCON, NT R345W and 1 μM ASO-treated R345W iRPE cultured
359 on chamber slides were analysed for BODIPY, APOE, COL4 and F3 expression and
360 localisation. Consistent with our earlier findings, ISCOCON iRPE show minimal
361 BODIPY and APOE signal (Figure 7A), indicating low lipid and APOE accumulation.
362 Conversely, the R345W NT condition exhibited strong immunostaining for both
363 markers. ASO1.1 treatment (1 μM) in R345W iRPE significantly reduced both BODIPY
364 and APOE fluorescence (Figure 7A, C, D). IF was also conducted with antibodies to
365 COL4 and F3 (Figure 7B). ISOCON iRPE showed a homogenous distribution of COL4
366 staining, in contrast to uneven patches of accumulated COL4 observed in the NT
367 R345W condition (Figure 7B). ASO1.1 treatment significantly attenuated COL4

368 accumulation, resulting in a more even staining pattern (Figure 7B, E), supporting a
369 potential role for mitigating ECM disorganisation induced by R345W *EFEMP1*
370 expression. These findings indicate that reduction of R345W *EFEMP1* expression not
371 only attenuates lipid and APOE accumulation, but also promotes the rescue of
372 pathological ECM features in DHRD iRPE.
373 Finally, TEM of ISOCON, NT R345W and ASO1.1-treated R345W iRPE was
374 conducted at day 158 following 2-month ASO1.1 gymnosis (1 μM) commencing at day
375 100 of differentiation. All cells showed characteristic RPE-like morphology, forming
376 monolayers of polarized pigmented cells (Figure 7F). Accumulation of microfibrils
377 (blue outline) was observed in the ISOCON iRPE between the basal membrane and
378 underlying transwell membrane (24% of surface) (Figure 7G). In contrast, lipid-rich
379 deposits (blue outline) were observed in the NT R345W-iPSC (22% of surface) with
380 microfibril accumulation in the extracellular matrix observed only rarely (5% of surface)
381 (Figure 7G). Lipid-rich deposits were almost completely absent (3% of surface) from
382 R345W iRPE following 2-month gymnosis with ASO1.1 (1 μM) (Figure 7G).
383
384 DISCUSSION
385 In this study, we confirm that both patient-derived and isogenic iRPE initially exhibit a
386 typical RPE-like morphology and express key RPE markers associated with epithelial
387 identity and polarity, tight junction formation and melanosome biogenesis. However,
388 the c.1033C>T, p.Arg(345Trp) variant results in progressive phenotypic alterations in
389 the patient-derived iRPE. While the corrected isogenic iRPE formed a well-organised,
390 uniform monolayer, the patient-derived iRPE fail to form a uniform monolayer and
391 become progressively less well-organised, with tight junctions appearing more
392 fragmented and discontinuous. Moreover, the basement membrane in the isogenic

393 control iRPE is well-organised, forming a continuous and uniform basal layer. In
394 contrast, a dysmorphic basal layer characterised by progressive disruption and
395 structural disorganisation of the extracellular matrix and thickening of the basement
396 membrane is evident in the patient-derived iRPE, indicating abnormalities in the
397 structural integrity of this layer. Interestingly, EFEMP1 itself is localised across the
398 basement membrane in both isogenic and patient-derived iRPE. However, in patient-
399 derived iRPE, EFEMP1 accumulated in the basement membrane and presented a
400 more filamentous appearance. This is consistent with the accumulation of EFEMP1
401 seen in the basal layer between RPE and drusen in human DHRD donor eyes, the
402 formation of basal deposits in primary mouse RPE cells carrying the R345W *Efemp1*
403 substitution and with the formation of sub-RPE deposits in R345W *Efemp1* knock-in
404 mice.[7,8,11] Finally, the accumulation of lipids and APOE, a key component of drusen,
405 is evident in the patient-derived iRPE. While lipid-rich deposits underneath the RPE in
406 the basal layer were seldom observed in the isogenic iRPE, increased sub-RPE lipid-
407 rich deposits were observed in the patient-derived iRPE. Similar phenotypic
408 characteristics have been reported in other models of DHRD using patient-derived
409 iRPE and isogenic controls.[13,14] Galloway *et al*. (2017) reported an increased
410 accumulation of lipids and APOE-positive basal deposits beneath the RPE in patient-
411 derived iRPE, in addition to increased deposition and levels of extracellular matrix and
412 basement membrane constituents.[13] Similarly, Tsai *et al*. (2021) reported the
413 intracellular and extracellular accumulation of lipids in patient-derived iRPE, in addition
414 to the downregulation of carboxylesterase 1 (CES1) and the attenuation of cholesterol
415 efflux from these cells.[14] The authors proposed that a hyper-inhibitory effect of R345W
416 EFEMP1 on epidermal growth factor receptor (EGFR) signaling may suppress CES1
417 expression, thereby attenuating cholesterol export and leading to lipid accumulation.

418

419 In addition to the phenotypic alterations described above, altered mitochondrial
420 morphology is a novel phenotype observed in the patient-derived iRPE, including a
421 population of elongated mitochondria and for some mitochondria, a longitudinal
422 orientation of the cristae. Mitochondrial dysfunction, together with oxidative stress and
423 inflammation, is increased in age-related macular degeneration (AMD),[23-25] but has
424 not been previously reported in juvenile macular dystrophy, raising the possibility of a
425 direct role for mitochondrial dysfunction in the disease pathology of these disorders.
426 Another novel finding in our study was the occurrence of microfibrils in the extracellular
427 matrix beneath the basement membrane in the isogenic iRPE which was largely
428 absent from the patient-derived iRPE. The ultrastructural appearance and banded
429 pattern of these microfibrils in the extracellular matrix suggest that they may be
430 comprised of collagen VI.[26] While the identity of these microfibrils in the extracellular
431 matrix requires further scrutiny, it has been reported that ARPE-19 cells engineered
432 to be homozygous for the R345W *EFEMP1* variant developed changes in the
433 extracellular matrix that included a reduced and disorganised network of stretched
434 collagen VI fibers in comparison to wild type ARPE-19, which exhibited a continuous
435 network of fibers with some thickened and localized areas.[27] This was accompanied
436 by a thickened and multilayered fibronectin network in the R345W ARPE-19 cells.[27]
437 Overall, the data are consistent with structural disorganisation of the extracellular
438 matrix in cellular models of DHRD.

439

440 Interestingly, the isogenic *EFEMP1* knockout iRPE in our study did not emulate the
441 phenotypic characteristics observed in the patient-derived iRPE. The *EFEMP1*
442 knockout iRPE formed a well-organised monolayer with a continuous and uniform

443 basement membrane indicating maintenance of the structural integrity of the
444 extracellular matrix. Moreover, APOE accumulation was not observed in the *EFEMP1*
445 knockout iRPE. Although this finding cannot fully rule out subtle or undetected
446 changes in the RPE basal layer and extracellular matrix, it does confirm the dominant
447 toxic gain-of-function of R345W EFEMP1 in the RPE in addition to the absence of
448 *EFEMP1* loss-of-function or haploinsufficiency as a disease mechanism underpinning
449 DHRD pathology.
450
451 Given the toxic gain-of-function of R345W EFEMP1, we designed an antisense
452 oligonucleotide to specifically promote the downregulation of the R345W *EFEMP1*
453 transcript through RNase H dependent degradation. Both assisted delivery of the lead
454 therapeutic ASO at a dose of 200 nM and gymnotic delivery over a dose range of 0.5
455 μM to 10 μM resulted in allele-specific targeting of the R345W *EFEMP1* transcript in
456 the patient-derived iRPE. ASO treatment of patient-derived iRPE through transient
457 transfection resulted in the reduction of R345W *EFEMP1* transcript levels to 11.7-
458 15.6% of total allelic expression as quantified by next generation sequencing, whilst
459 gymnotic treatment was less effective, reducing R345W *EFEMP1* transcript levels to
460 22-27% of total levels. A dose-dependent response was not observed following
461 gymnotic delivery of the lead ASO, with the magnitude of knockdown of the R345W
462 *EFEMP1* transcript comparable between the lowest and highest ASO doses tested,
463 indicating that maximal target suppression could be achieved at or below the lowest
464 tested concentration. Despite the reduced efficacy of the lead ASO to reduce the
465 R345W *EFEMP1* transcript following gymnotic delivery, treatment of patient-derived
466 iRPE with the lead ASO was able to effectively rescue the disease phenotype even
467 when treatment was initiated after the onset of the phenotypic changes and within a

468 short treatment timeframe. A one-week gymnotic treatment with ASO resulted in
469 substantial reduction in drusen-associated APOE accumulation. Similarly, a two-week
470 gymnotic ASO treatment administered after progression of the phenotypic changes in
471 the patient-derived iRPE resulted in a pronounced reduction not only of APOE, but
472 also lipid accumulation. Finally, a two-month gymnotic treatment in aged patient-
473 derived iRPE was shown to not only attenuate APOE and sub-RPE lipid deposits but
474 also rescue the disorganisation of the extracellular matrix. These results suggest that
475 administration of ASO treatment after the onset of drusen formation in DHRD patients
476 could be therapeutically beneficial in ameliorating the pathological features of the
477 disease.
478
479 While no therapeutic oligonucleotide has been shown to be effective for the treatment
480 of DHRD to date, AMD has been demonstrated to be amenable to administration of
481 oligonucleotide therapies via intravitreal administration. Pegaptanib (MacugenTM)
482 and avacincaptad pegol (IzervayTM) are small oligonucleotide RNA aptamers
483 approved for the treatment of AMD.[28] Macugen is an anti-angiogenic therapy targeting
484 vascular endothelial growth factor (VEGF) for the treatment of neovascular AMD
485 granted FDA approval in 2004 and EMA approval in 2006, while Izervay targets
486 complement C5 for the treatment of geographic atrophy secondary to AMD and was
487 approved by the FDA in 2023. The biological mechanisms of these aptamers differ
488 from that of the antisense oligonucleotide investigated in this study. Macugen blocks
489 the biological activity of VEGF by binding selectively to the exon 7-encoded heparin-
490 binding domain of the VEGF-165 isoform thereby preventing interaction with its
491 receptors. Izervay targets the complement system by blocking the cleavage of the C5
492 complement protein into C5a and C5b preventing the assembly of the membrane

493 attack complex (MAC). The route of aptamer administration for these approved
494 therapies includes intravitreal injection or scleral injection via the inferotemporal
495 quadrant. Several other aptamers are currently under clinical investigation for the
496 treatment of AMD, including E10030 (Fovista®), umedaptanib pegol (APT-F2P, RBM-
497 007) and AS1411.[28] Moreover, several small interfering RNA (siRNA)-mediated
498 therapies for neovascular AMD are under clinical investigation.[29] Only one antisense
499 oligonucleotide therapy has entered clinical trials for the treatment of AMD. The safety
500 and pharmacodynamic profile of Sefaxersen (RO7434656), a GalNAc-conjugated 2'-
501 MOE antisense oligonucleotide targeting hepatic complement factor B mRNA, has
502 been investigated in a phase 1 study involving single or repeated subcutaneous
503 administration of the drug, with a view to treat geographic atrophy secondary to AMD.[30]
504
505 Despite the complex aetiology of AMD, there is a significant overlap in pathological
506 features between DHRD and AMD, including the drusen-associated accumulation of
507 EFEMP1 in AMD patients.[9,31] Therapeutic oligonucleotides developed for the
508 treatment of AMD have not been investigated for the overlapping indications in DHRD.
509 Currently, the clinical care of DHRD patients includes the use of low-vision aides to
510 assist with daily living, and regular observation and retinal imaging to monitor drusen
511 and detect complications such as choroidal neovascularisation (CNV). Interventions
512 targeting complications that occur in some DHRD patients, including anti-VEGF
513 injections (bevacizumab or ranibizumab) for CNV, photodynamic laser therapy and
514 low-energy subthreshold nanosecond laser (2RT) treatment, have been trialled in a
515 small number of DHRD patients.[32,33] In comparison, our antisense oligonucleotide is
516 the first to target the cause of DHRD at source and could potentially be used to treat
517 all DHRD patients. Although DHRD is rare (c.1033C>T variant allele frequency of 1.23

518 × 10^{-5} in gnomAD database v4.1.0), it is a monogenic, single variant disorder with all
519 DHRD patients worldwide harbouring the *EFEMP1* c.1033C>T, p.Arg(345Trp) variant.
520 In an investigation of the spectrum of genetic variants in the most common genes
521 causing inherited retinal disease in a large molecularly characterized cohort in the
522 United Kingdom, the *EFEMP1* c.1033C>T, p.Arg(345Trp) variant was identified as one
523 of the top twenty most prevalent variants identified.[34] We conclude that our allele-
524 specific antisense oligonucleotide could be a viable therapeutic option for DHRD
525 patients, with the potential to alleviate the underlying pathology, including sub-RPE
526 deposition of drusen-associated components and structural reorganisation of the RPE
527 extracellular matrix, ultimately improving clinical outcomes.
528
529 MATERIALS & METHODS
530 **EFEMP1 plasmids**
531 *EFEMP1* (ENST00000355426.8) was amplified from cDNA prepared from retinal
532 organoids as described in Sai *et al*. (2024).[35] USER cloning technology (NEB, Hitchin,
533 UK) was used according to the manufacturer's instructions to insert the *EFEMP1* open
534 reading frame excluding the stop codon into the mammalian expression vector
535 p3xFLAG-CMV-14 (E7908) from Merck (Sigma-Aldrich, Gillingham, UK) and
536 pmScarlet_C1 (Addgene, plasmid #85042), resulting in in-frame fusion of EFEMP1
537 with a C-terminal 3xFLAG tag (pEFEMP1-3xFLAG) and C-terminal mScarlet tag
538 (pEFEMP1-mScarlet) respectively. The *EFEMP1* c.1033C>T, p.Arg(345Trp) variant
539 and a Kozak sequence upstream of the *EFEMP1* open reading frame were introduced
540 into pEFEMP1-mScarlet by site directed mutagenesis using the Q5 Site Directed
541 Mutagenesis Kit (NEB) to generate pEFEMP1(R345W)-mScarlet. Primer sequences
542 for *EFEMP1* amplification and sequencing are in Supplemental Table 5.

543 **ASO screening in HEK293T cells**

544 HEK293 cells (ATCC) were cultured with DMEM (Life Technologies, Waltham, MA,
545 USA) with 10% fetal bovine serum (Invitrogen, Thermo Fisher Scientific, Paisley, UK)
546 at 37°C with 5% CO_2. HEK293T cells were seeded in 24-well plates at a density of 0.7
547 × 10^5 cells per well and transfected 24 hours later using Lipofectamine 2000
548 (Invitrogen, Thermo Fisher Scientific) as described by the manufacturer. HEK293T
549 cells were transfected with both pEFEMP1(WT)-3xFLAG (800 ng) and
550 pEFEMP1(R345W)-mScarlet (800 ng), and with control ASO (CTRL) (50 nM) or
551 increasing concentrations (25 nM, 50 nM, 100 nM, 200 nM) of therapeutic ASO.
552 Results were compared to untreated cells transfected with both plasmids (plasmids
553 only). The RNA was extracted 48 hours post-treatment with the RNeasy Mini Kit
554 (Qiagen, Manchester, UK) and cDNA synthesised from RNA samples using the Tetro
555 cDNA Synthesis Kit (Bioline, Meridian Bioscience Europe, London, UK) according to
556 the manufacturer's protocol. Quantitative PCR (qPCR) was conducted using primer
557 pairs specific for WT *EFEMP1,* R345W *EFEMP1* or total *EFEMP1* to quantify the
558 levels of *EFEMP1* transcript using an Applied Biosystems QuantStudioTM 6 Flex real-
559 time PCR system and the ΔΔCt method. Gene expression was normalized to the
560 housekeeping genes *GAPDH* and *ACTB* and all values were expressed relative to the
561 untreated 'plasmid only' condition. Primer sequences for *EFEMP1* qPCR are in
562 Supplemental Table 5.

563 **Urine collection and renal epithelial cell isolation and expansion**

564 Urine was collected from a DHRD patient harbouring the c.1033C>T, p.Arg(345Trp)
565 variant in *EFEMP1*. Collection, isolation and expansion of renal epithelial cells was
566 carried out similarly to protocols described by Zhou *et al.* (2012) and Hildebrand *et al.*
567 (2016).[36,37] Briefly, the urine sample (around 50 ml) was centrifuged at 400g for 10

568 minutes. The supernatant was discarded, and the pellet was washed with 10 ml of
569 Dulbecco's phosphate-buffered saline (Thermo Fisher Scientific) containing 1x Anti-
570 Anti (Thermo Fisher Scientific) and centrifuged at 400g for 10 minutes. The pellet was
571 resuspended in 2 ml of Primary Medium, consisting of DMEM/Ham's F-12 nutrient mix
572 (1:1) (Thermo Fisher Scientific), with 10% of fetal bovine serum (FBS; Thermo Fisher
573 Scientific), Renal Cell Growth Medium (REGM) SingleQuot kit supplements (Lonza,
574 Cambridge, UK) and 1x Anti-Anti. The cells were seeded into a single well of a 12-well
575 plate coated with 0.1% gelatin. 1 ml of primary medium was added to the well at 24,
576 48 and 72 hours following plating, without removal of any media. Renal epithelial cell
577 colonies appeared within 3 days. 96 hours post-seeding, most of the medium was
578 aspirated and replaced by Proliferation Medium, consisting of a 1:1 mixture of Renal
579 Epithelial Cell Growth Basal Medium (REBM) medium supplemented with REGM
580 SingleQuots (Lonza) and DMEM high glucose (Thermo Fisher Scientific)
581 supplemented with 10% FBS, 1% GlutaMAX, 1% non-essential amino acids (NEAA)
582 and 1x Anti-Anti. Half media changes were performed every day. 14 days following
583 urine collection, cells reached 90% density and were dissociated using TrypLE
584 Express (Thermo Fisher Scientific) for 10 minutes at 37°C, before being seeded at a
585 ratio of 1:4 onto gelatin coated wells. Cells were expanded for a maximum of four
586 passages.

587 **Human iPSC reprogramming and culture**

588 Renal epithelial cells passaged less than 3 times were used to generate iPSCs. 5 x
589 10^5 cells were dissociated using TrypLE Express (Thermo Fisher Scientific) for 10
590 minutes at 37°C and electroporated with four integration-free episomal vectors:
591 pCXLE-hOCT3/4-shp53-F (Addgene, plasmid #27077, pCXLEhSK (Addgene,
592 plasmid #27078) containing SOX2 and KLF4, pCXLEhUL (Addgene, plasmid #27080)

593 containing L-MYC and LIN28, and miRNA 302/367 plasmid (Gift from Dr J. A.
594 Thomson, Regenerative Biology, Morgridge Institute for Research, Madison,
595 Wisconsin, USA; Howden et al., 2015) using the AmaxaTM Basic NucleofectorTM Kit
596 for primary mammalian epithelial cells, program T-020 (Lonza). Electroporated cells
597 were seeded onto 1% Geltrex-coated (Thermo Fisher Scientific) plates and cultured
598 in StemFlex media (Thermo Fisher Scientific). Media changes were carried out every
599 other day. iPSC colonies were picked around day 14, expanded in Stem Flex media
600 on Geltrex-coated 6-well plates and routinely passaged using Cell Dissociation Buffer
601 (Thermo Fisher Scientific). iPSC line pluripotency was confirmed using iPSC-specific
602 antibodies: anti-OCT4 (Abcam, Cambridge, UK), anti-Nanog (Abcam), anti SSEA4
603 (Cell Signalling Technologies, Cambridge, UK) and anti-TRA-1-80 (Invitrogen, Thermo
604 Fisher Scientific) (Table S6).

605 **Generation of isogenic iPSC lines**

606 To generate an isogenic control line (ISOCON), a 20nt gRNA (NGG PAM) and 127nt
607 single stranded oligo deoxynucleotide (ssODN) template were designed for the
608 correction of the *EFEMP1* c.1033C>T allele through CRISPR-mediated homology-
609 directed repair (HDR). The ssODN repair template incorporated the desired correction
610 and a synonymous PAM change to prevent further Cas9-mediated cleavage of the
611 edited DNA. To generate an *EFEMP1* knock out (ISOKO) iPSC line, CRISPR-
612 mediated non-homologous end joining (NHEJ) in the patient iPSC line was employed.
613 A 20 nt gRNA with a canonical PAM (NGG) was designed to target exon 5 of *EFEMP1*
614 (Table S2). The CRISPR RNA (crRNA) and ssODN (with phosphorothioate (PS)
615 modifications to the ends) reagents were obtained from Integrated DNA Technologies
616 (IDT, Bristol, UK). Sequences for crRNAs and ssODNs are in Supplementary Table 1
617 and 2 (Table S1 and S2). Trans-activating CRISPR RNA (tracrRNA), crRNA and

618 ssDNA donors were resuspended in nuclease-free ddH_2O to 100 μM. The crRNA and
619 tracrRNA were combined and heated at 95°C for 5 minutes to form a 50 μM gRNA
620 complex. 3 μl of gRNA complexes were then added to 2 μL of 61 μM Alt-R Cas9
621 enzyme (IDT) to generate ribonucleoprotein (RNP) complexes and incubated at room
622 temperature (RT) for 20 minutes. iPSCs were cultured in Stemflex (Gibco, Thermo
623 Fisher Scientific) with 10 uM ROCK inhibitor Y-27632 (STEMCell Technologies,
624 Cambridge, UK) for 2 hours prior to single-cell dissociation with TrypLE (Gibco,
625 Thermo Fisher Scientific). The dissociated cells (2×10^5 cells per reaction) were
626 centrifuged at 200g for 5 minutes and resuspended in P3 Primary cell nucleofector
627 solution (Lonza) prior to the addition of 5 μl RNP solution, 2 μl of 100 μM ssODN (for
628 CRISPR correction) and 4 μl Electroporation Enhancer. The iPSC-RNP mix was
629 nucleofected using a P3 Primary Cell 4D-Nucleofector X Kit S (Lonza) using program
630 CA-137. iPSC clones were expanded, and individual clones were mechanically
631 isolated and plated into individual wells of a Geltrex-coated 12-well plate. Clonal iPSC
632 lines were expanded and screened for the desired edit by Sanger sequencing (Source
633 Bioscience).

634 **RPE differentiation**

635 iPSCs were cultured to 90–100% confluency on Geltrex-coated plates (Thermo Fisher
636 Scientific) and then directed to differentiate into retinal pigment epithelial (RPE) cells
637 following the protocol described by Regent *et al.* (2019).[20] The RPE differentiation
638 medium comprised high-glucose Dulbecco's modified Eagle's medium (Thermo Fisher
639 Scientific), supplemented with 50 μM β-mercaptoethanol (Thermo Fisher Scientific),
640 1× minimum essential medium–nonessential amino acids (Thermo Fisher Scientific),
641 and knockout serum replacement (KSR, Thermo Fisher Scientific) at 20% from day 0
642 to day 50, which was reduced to 4% after passage 1. Additional supplements included

643 10 mM nicotinamide (Sigma-Aldrich) from days 0 to 7, 100 ng/ml Activin A (PeproTech,
644 London, UK) from days 7 to 14, and 3 μM CHIR99021 (Cell Guidance Systems,
645 Cambridge, UK) until passage 1. Media changes were carried out every 2 to 3
646 days. Around day 50, cells were treated with TrypLE Express Reagent (Thermo Fisher
647 Scientific) at 37°C for 10 minutes. Visibly pigmented patches were manually isolated,
648 and cells were further incubated for up to one hour with TrypLE Express to ensure
649 dissociation. Finally, cells were seeded onto Geltrex-coated plates at a density of
650 100,000 cells per cm² for subsequent experiments.

651 **Antisense oligonucleotide gymnosis**

652 Gymnotic ASO experiments took place by adding the desired ASO concentration into
653 the media once a week. Half media changes were carried out 3 days later, with no
654 ASO added.

655 **Immunostaining**

656 iRPE monolayers grown in 12-well plates were washed with DPBS (Thermo Fisher
657 Scientific) and were carefully removed using a cell scraper and transferred to bijou
658 tubes where they were fixed in 4% paraformaldehyde (Thermo Fisher Scientific) for
659 10 mins at RT. The iRPE were washed 3x in DPBS and following the last wash, were
660 incubated in 30% sucrose at 4°C overnight. iRPE monolayers were vertically
661 embedded in OCT compound (CellPath, Newtown, UK) and frozen on dry ice. Blocks
662 were stored at -80°C prior to sectioning at 14 μm onto charged slides using a Leica
663 CM1850 cryostat. Cells grown on chamber slides were washed with PBS (Thermo
664 Fisher Scientific) and fixed in 4% paraformaldehyde (Thermo Fisher Scientific) for 10
665 mins at RT. Cells grown in chamber slides and vertically-embedded iRPE were
666 permeabilised using 0.1% TritonX100 (Sigma-Aldrich) for 15 minutes before being
667 blocked using a solution containing 0.3% bovine serum albumin (BSA, Sigma-Aldrich),

668 10% FBS (Thermo Fisher Scientific) for 1 hour at RT. Primary antibodies (Table S6)
669 were diluted at the appropriate concentration in blocking solution and incubated for 1
670 hour at RT. Samples were washed 3x with PBS (Thermo Fisher Scientific) and
671 subsequently incubated with secondary antibodies (Table S7) that reacted against the
672 primary antibody species for 1 hour at RT, before being washed 3x with PBS. For
673 BODIPY 493/503 (Thermo Fisher Scientific) staining, samples were incubated for 15
674 minutes using a 10 mM BODIPY stock that was diluted 1:1000 following 2x washes
675 with PBS. All samples were incubated with 4,6-diamidino-2-phenylindole (DAPI; 2
676 mg/mL) (Invitrogen, Thermo Fisher Scientific) in PBS for 5 minutes, then washed 3x
677 with PBS. Slides were mounted in fluorescence mounting media (Dako, Agilent, CA,
678 USA). All images were acquired using a Zeiss LSM700 Confocal Microscope and
679 prepared using ImageJ, Adobe Photoshop and Adobe Illustrator.

680 **Western blotting**

681 iRPE were washed with PBS and lysed on ice for 30 minutes in 80-120µl cold RIPA
682 buffer (50mM Tris HCL, pH 7.5; 150mM NaCl; 1mM EDTA; 1% NP-40; 0.5% sodium
683 deoxycholate; 0,1% SDS) supplemented with 2% protease inhibitor cocktail (Sigma-
684 Aldrich). The samples were briefly sonicated before centrifuging at 4°C for 1 minute at
685 13k RPM. Protein concentration was quantified using Pierce BCA Protein Assay kit
686 (Thermo Fisher Scientific) as per manufacturer's instructions. Protein samples (20 µg)
687 were mixed with 4x sample buffer before being heated at 100°C for 3 minutes to
688 facilitate protein denaturation. Samples were resolved on precast 4–20% gradient gels
689 (Bio-Rad, Watford, UK) at 100 V until the dye reached the end of the gel. Pageruler
690 Plus protein ladder (Thermo Fisher Scientific) was used to provide a reference for
691 protein size. Proteins were transferred to a nitrocellulose membrane by wet transfer
692 for 90 minutes, using standard protocols. Membranes were blocked overnight at 4°C

693 in 5% skimmed milk powder in PBS + 0.1%Tween-20 (PBS-T), then incubated for 1
694 hour in primary antibody, before undergoing 3x 10-minute washes with PBS-T.
695 Membranes were then incubated in species-specific HRP-conjugated secondary
696 antibody for 1 hour before undergoing 3x 10-minute washes with PBS-T. All antibodies
697 are listed in supplemental table 6 and 7 (Table S6). Membranes were developed using
698 Clarity MAX Western ECL (Bio-Rad) for 5 min. Membranes were imaged using a
699 ChemiDoc MP Imaging System (Bio-Rad). Images were formatted using Image Lab
700 (Bio-Rad). Three independent protein isolates were used per condition.

701 **Transmission electron microscopy**

702 iRPE cells cultured on transwell filters were fixed in EM fixative (2% gluteraldehyde,
703 2% paraformaldehyde in 0.1M sodium cacodylate buffer, pH 7.4) for 30 min at room
704 temperature and post-fixed with 1% osmium tetroxide/1.5% potassium ferricyanide in
705 0.1 M sodium cacodylate buffer for 1 hour at 4°C. Cells were stained with 2% uranyl
706 acetate replacement solution (UA Zero) for 1 hour, dehydrated through an ethanol
707 series, and infiltrated with TAAB-812 epoxy resin (TAAB Laboratories, Aldermaston,
708 UK) prior to polymerization overnight at 60°C. Ultrathin sections were imaged on a
709 JEOL 1400Plus EM (JEOL ltd, Tokyo, Japan) fitted with an Advanced Microscopy
710 Technologies (AMT) NanoSprint12 camera (AMT Imaging Direct, Woburn, MA, USA).
711 Quantitation of accumulations between the basal membrane and underlying transwell
712 membrane was conducted manually and blind to the condition. ISOCON iRPE, 40
713 cells (~10 µm/cell); R345W iRPE, 25 cells (~ 7.8 µm/cell); ASO1.1-treated R345W
714 iRPE, 22 cells (~9.7 µm/cell).

715 **Processing of DNA and RNA from iRPE**

716 Total gDNA from cell samples was extracted using the Wizard gDNA Purification Kit

717 (Promega) following the manufacturer's guidelines. Total RNA from cell samples was
718 extracted using the RNeasy Micro Kit (Qiagen) following the manufacturer's
719 guidelines. cDNA was synthesised (Tetro cDNA synthesis, Bioline) using equal
720 quantities of total RNA for each sample (1 µg) and carried out according to the
721 manufacturer's guidelines.

722 **Quantitative PCR (qPCR) of iRPE samples**

723 qPCR was used to determine relative levels of *EFEMP1* gene expression (normalised
724 to the housekeeping genes *ACTB* and *GAPDH*), by measuring the fluorescence
725 emitted by DNA bound to the intercalating dye SYBR green. qPCR reactions were
726 assembled using 2x LabTaq Green Hi Rox Master Mix (Labtech, Heathfield, UK) and
727 conducted with an Applied Biosystems QuantStudio ™ 6 Flex real-time PCR system.

728 **Next generation sequencing**

729 Universal tagged primers for MiSeq (Illumina) high-throughput sequencing (HTS) are
730 listed in Supplemental Table 5 (Table S5). PCR amplification was carried out using
731 High-Fidelity 2x master mix (NEB). Products were gel-extracted (Monarch® DNA Gel
732 Extraction Kit, NEB) and 300-500ng of product used for subsequent steps. Processing
733 of the samples using MiSeq Reagent Nano Kit v2 was carried out at the UCL Cancer
734 Institute CAGE Facility.

735 **Data visualisation and statistical analysis**

736 Statistical analyses were carried out using RStudio (R v4.2.1). One way ANOVAs were
737 carried out using the base R aov function and post-hoc analyses using the RStudio
738 package rstatix (v0.7.2). All graphs presented were generated using the RStudio
739 package using the RStudio package ggplot2 (v3.4.1).

740

741 DATA AVAILABILITY

742 The data related to this study are fully documented in the paper or in the Supplemental
743 materials.
744
745 ACKNOWLEDGEMENTS
746
747 The authors gratefully acknowledge funding from the Macular Society (20-RG-04 to
748 J.v.d.S (PI), A.-J.F.C. (Co-I), M.E.C. (Co-I) and M.M. (Co-I)). This research was
749 supported by the National Institute for Health and Care Research Biomedical
750 Research Centre at Moorfields Eye Hospital and UCL Institute of Ophthalmology and
751 the Wellcome Trust (099173/Z/12/Z to M.M. and 205041/Z/16/Z to M.E.C.).
752 pmScarlet_C1 was a gift from Dorus Gadella (Addgene plasmid # 85042). miRNA
753 302/367 plasmid was a gift from Dr J. A. Thomson, Regenerative Biology, Morgridge
754 Institute for Research, Madison, Wisconsin, USA (Howden et al., 2015). pCXLE-
755 hOCT3/4-shp53-F (Addgene, plasmid #27077), pCXLEhSK (Addgene, plasmid
756 #27078) and pCXLEhUL (Addgene, plasmid #27080) were a gift from Shinya
757 Yamanaka. We thank the Cancer Genomics Engineering (CAGE) Facility, UCL
758 Cancer Institute, for the MiSeq preparation and sequencing. The CAGE Facility is
759 supported by the BRC, Welton Foundation and in part by the Cancer Research UK –
760 UCL Centre.
761
762 AUTHOR CONTRIBUTIONS
763 Conceptualization, J.v.d.S.; Data curation, F.O.R.; E.R.E.; J.v.d.S.; Formal analysis,
764 F.O.R.; B.S-P.; E.R.E., J.v.d.S.; Funding Acquisition, J.v.d.S.; A-J.F.F.; M.E.C.; M.M.
765 Investigation, F.O.R.; B.S-P.; E.R.E.; Methodology, F.O.R.; B.S-P.; E.R.E.; J.v.d.S.;
766 Project Administration, J.v.d.S.; Resources, N.A.; A.R.W.; A.-J.F.C; M.E.C.; M.M.;

767 Supervision, J.v.d.S; Software, F.O.R.; Validation, F.O.R.; B.S-P.; E.R.E., J.v.d.S;
768 Visualization; F.O.R.; B.S-P.; E.R.E., J.v.d.S.; Writing – original draft; F.O.R.; J.v.d.S.;
769 Writing – review and editing, F.O.R.; B.S-P.; E.R.E., N.A.; A.R.W.; A.-J.F.C; M.E.C.;
770 M.M.; J.v.d.S.
771
772 DECLARATION OF INTERESTS
773
774 An international patent application (PCT/GB2024/052082) related to this work has
775 been filed in collaboration with UCL Business Ltd. (UCLB). J.v.d.S, F.O.R. and B.S.-
776 P. are listed as inventors on this application.
777
778 KEYWORDS (5-10)
779 Doyne honeycomb retinal dystrophy, EFEMP1, inherited macular degeneration,
780 antisense oligonucleotide, retinal pigment epithelium, drusen
781
782 REFERENCES
783 1. Michaelides, M., Jenkins, S.A., Brantley, M.A., Jr, Andrews, R.M., Waseem, N.,
784 Luong, V., Gregory-Evans, K., Bhattacharya, S.S., Fitzke, F.W., Webster, A.R. (2006).
785 Maculopathy due to the R345W substitution in fibulin-3: distinct clinical features,
786 disease variability, and extent of retinal dysfunction. Invest. Ophthalmol. Vis.
787 Sci. *47*(7), 3085–3097.
788
789 2. Zech, J.C., Zaouche, S., Mourier, F., Placuchu, H., Grange, J. D., Trepsat, C.
790 (1999). Macular dystrophy of malattia leventinese. A 25 year follow up. Br. J.
791 Ophthalmol. *83*(10), 1195–1196.

3. de Guimarães, T.A.C., Kalitzeos, A., Mahroo, O.A., van der Spuy, J., Webster, A.R., Michaelides, M. (2024). A Long-Term Retrospective Natural History Study of EFEMP1-Associated Autosomal Dominant Drusen. Invest. Ophthalmol. Vis. Sci. *65*(6), 31.

4. Stone, E.M., Lotery, A. J., Munier, F.L., Héon, E., Piguet, B., Guymer, R.H., Vandenburgh, K., Cousin, P., Nishimura, D., Swiderski, R.E., et al. (1999). A single EFEMP1 mutation associated with both Malattia Leventinese and Doyne honeycomb retinal dystrophy. Nat. Genet. *22*(2), 199–202.

5. Hulleman, J.D., Kelly, J.W. (2015). Genetic ablation of N-linked glycosylation reveals two key folding pathways for R345W fibulin-3, a secreted protein associated with retinal degeneration. FASEB J. *29*(2), 565–575.

6. Woodard, D.R., Daniel, S., Nakahara, E., Abbas, A., DiCesare, S.M., Collier, G.E., Hulleman, J.D. (2022). A loss-of-function cysteine mutant in fibulin-3 (EFEMP1) forms aberrant extracellular disulfide-linked homodimers and alters extracellular matrix composition. Hum. Mutat. *43*(12), 1945–1955.

7. Marmorstein, L.Y., Munier, F.L., Arsenijevic, Y., Schorderet, D.F., McLaughlin, P.J., Chung, D., Traboulsi, E., Marmorstein, A.D. (2002). Aberrant accumulation of EFEMP1 underlies drusen formation in Malattia Leventinese and age-related macular degeneration. Proc. Natl. Acad. Sci. U S A. *99*(20), 13067–13072.

817 8. Marmorstein, L.Y., McLaughlin, P.J., Peachey, N.S., Sasaki, T., Marmorstein, A.D.
818 (2007). Formation and progression of sub-retinal pigment epithelium deposits in
819 Efemp1 mutation knock-in mice: a model for the early pathogenic course of macular
820 degeneration. Hum. Mol. Genet. *16*(20), 2423–2432.
821
822 9. Klenotic, P.A., Munier, F.L., Marmorstein, L.Y., Anand-Apte, B. (2004). Tissue
823 inhibitor of metalloproteinases-3 (TIMP-3) is a binding partner of epithelial growth
824 factor-containing fibulin-like extracellular matrix protein 1 (EFEMP1). Implications for
825 macular degenerations. J. Biol. Chem. *279*(29), 30469–30473.
826
827 10. Zayas-Santiago, A., Cross, S.D., Stanton, J.B., Marmorstein, A.D., Marmorstein,
828 L.Y. (2017). Mutant Fibulin-3 Causes Proteoglycan Accumulation and Impaired
829 Diffusion Across Bruch's Membrane. Invest. Ophthalmol. Vis. Sci. *58*(7), 3046–3054.
830
831 11. Fernandez-Godino, R., Garland, D.L., Pierce, E.A. (2015). A local complement
832 response by RPE causes early-stage macular degeneration. Hum. Mol.
833 Genet. *24*(19), 5555–5569.
834
835 12. Crowley, M.A., Garland, D.L., Sellner, H., Banks, A., Fan, L., Rejtar, T., Buchanan,
836 N., Delgado, O., Xu, Y.Y., Jose, S., et al. (2023). Complement factor B is critical for
837 sub-RPE deposit accumulation in a model of Doyne honeycomb retinal dystrophy with
838 features of age-related macular degeneration. Hum. Mol. Genet. *32*(2), 204–217.
839
840 13. Galloway, C.A., Dalvi, S., Hung, S.S.C., MacDonald, L.A., Latchney, L.R., Wong,
841 R.C.B., Guymer, R.H., Mackey, D.A., Williams, D.S., Chung, M.M., et al. (2017).

842 Drusen in patient-derived hiRPE models of macular dystrophies. Proc. Natl. Acad. Sci.
843 U S A. *114*(39), E8214–E8223.
844
845 14. Tsai, Y.T., Li, Y., Ryu, J., Su, P.Y., Cheng, C.H., Wu, W.H., Li, Y.S., Quinn, P.M.J.,
846 Leong, K.W., Tsang, S.H. (2021). Impaired cholesterol efflux in retinal pigment
847 epithelium of individuals with juvenile macular degeneration. Am. J. Hum.
848 Genet. *108*(5), 903–918.
849
850 15. Driver, S.G.W., Jackson, M.R., Richter, K., Tomlinson, P., Brockway, B., Halliday,
851 B.J., Markie, D.M., Robertson, S.P., Wade, E.M. (2020). Biallelic variants in EFEMP1
852 in a man with a pronounced connective tissue phenotype. Eur. J. Hum. Genet. *28*(4),
853 445–452.
854
855 16. McLaughlin, P.J., Bakall, B., Choi, J., Liu, Z., Sasaki, T., Davis, E.C., Marmorstein,
856 A.D., Marmorstein, L.Y. (2007). Lack of fibulin-3 causes early aging and herniation,
857 but not macular degeneration in mice. Hum. Mol. Genet. *16*(24), 3059–3070.
858
859 17. Stanton, J.B., Marmorstein, A.D., Zhang, Y., Marmorstein, L.Y. (2017). Deletion of
860 Efemp1 Is Protective Against the Development of Sub-RPE Deposits in Mouse
861 Eyes. Invest. Ophthalmol. Vis. Sci. *58*(3), 1455–1461.
862
863 18. Leung, A., Sacristan-Reviriego, A., Perdigão, P.R.L., Sai, H., Georgiou, M.,
864 Kalitzeos, A., Carr, A.F., Coffey, P.J., Michaelides, M., Bainbridge, J., et al. (2022).
865 Investigation of PTC124-mediated translational readthrough in a retinal organoid

model of AIPL1-associated Leber congenital amaurosis. Stem cell reports, *17*(10), 2187–2202.

19. Perdigão, P.R.L., Ollington, B., Sai, H., Leung, A., Sacristan-Reviriego, A., van der Spuy, J. (2023). Retinal Organoids from an AIPL1 CRISPR/Cas9 Knockout Cell Line Successfully Recapitulate the Molecular Features of LCA4 Disease. Int. J. Mol. Sci. *24*(6), 5912.

20. Regent, F., Morizur, L., Lesueur, L., Habeler, W., Plancheron, A., Ben M'Barek, K., Monville, C. (2019). Automation of human pluripotent stem cell differentiation toward retinal pigment epithelial cells for large-scale productions. Sci. Rep. *9*(1), 10646.

21. Slijkerman, R., Kremer, H., & van Wijk, E. (2018). Antisense Oligonucleotide Design and Evaluation of Splice-Modulating Properties Using Cell-Based Assays. Methods Mol. Biol. *1828*, 519–530

22. Liang, X.H., Sun, H., Nichols, J.G., Crooke, S.T. (2017). RNase H1-Dependent Antisense Oligonucleotides Are Robustly Active in Directing RNA Cleavage in Both the Cytoplasm and the Nucleus. Mol. Ther. *25*(9), 2075–2092.

23. Kaarniranta, K., Uusitalo, H., Blasiak, J., Felszeghy, S., Kannan, R., Kauppinen, A., Salminen, A., Sinha, D., Ferrington, D. (2020). Mechanisms of mitochondrial dysfunction and their impact on age-related macular degeneration. Prog. Retin. Eye Res. 79, 100858.

891

892 24. Fisher, C.R., Shaaeli, A.A., Ebeling, M.C., Montezuma, S.R., Ferrington, D.A.
893 (2022). Investigating mitochondrial fission, fusion, and autophagy in retinal pigment
894 epithelium from donors with age-related macular degeneration. Sci. Rep. *12*(1),
895 21725.
896

897 25. Datta, S., Cano, M., Ebrahimi, K., Wang, L., Handa, J.T. (2017). The impact of
898 oxidative stress and inflammation on RPE degeneration in non-neovascular
899 AMD. Prog. Retin. Eye Res. *60*, 201–218.
900

901 26. Knupp, C., Pinali, C., Munro, P.M., Gruber, H.E., Sherratt, M.J., Baldock, C.,
902 Squire, J.M. (2006) Structural correlation between collagen VI microfibrils and
903 collagen VI banded aggregates. J. Struct. Biol. *154*(3), 312-26.
904

905 27. Fernandez-Godino, R., Bujakowska, K.M., Pierce, E.A. (2018). Changes in
906 extracellular matrix cause RPE cells to make basal deposits and activate the
907 alternative complement pathway. Hum. Mol. Genet. *27*(1), 147–159.
908

909 28. Bege, M., Ghanem Kattoub, R., Borbás, A. (2025) The 20th Anniversary of
910 Pegaptanib (MacugenTM), the First Approved Aptamer Medicine: History, Recent
911 Advances and Future Prospects of Aptamers in Therapy. Pharmaceutics. *17*(3), 394.
912

913 29. Kumar, S., Fry, L.E., Wang, J.H., Martin, K.R., Hewitt, A.W., Chen, F.K., Liu, G.S.
914 (2023). RNA-targeting strategies as a platform for ocular gene therapy. Prog. Ret. Eye
915 Res. *92*, 101110.

916

917 30. McCaleb, M.L., Hughes, S.G., Grossman, T.R., Frazer-Abel, A., Jung, B., Yin, L.,
918 Henry, S.P., Monia, B.P., Schneider, E., Geary, R., et al. (2025). Inhibiting the
919 alternative pathway of complement by reducing systemic complement factor B:
920 Randomized, double-blind, placebo-controlled phase 1 studies with
921 Sefaxersen. Immunobiology. *230*(2), 152876.

922

923 31. Crabb, J.W., Miyagi, M., Gu, X., Shadrach, K., West, K.A., Sakaguchi, H., Kamei,
924 M., Hasan, A., Yan, L., Rayborn, M.E., et al. (2002). Drusen proteome analysis: an
925 approach to the etiology of age-related macular degeneration. Proc. Natl. Acad. Sci.
926 U S A. *99*(23), 14682–14687.

927

928 32. Cusumano, A., Falsini, B., Giardina, E., Cascella, R., Sebastiani, J., Marshall, J.
929 (2019). Doyne honeycomb retinal dystrophy - functional improvement following
930 subthreshold nanopulse laser treatment: a case report. J. Med. Case. Rep. *13*(1), 5.

931

932 33. Cusumano, A., Falsini, B., D'Ambrosio, M., D'Apolito, F., Sebastiani, J., Levialdi
933 Ghiron, J. H., Giardina, E., Cascella, R. (2023). Long-Term Structural and Functional
934 Assessment of Doyne Honeycomb Retinal Dystrophy following Nanosecond 2RT
935 Laser Treatment. Case Reports. Case Rep. Ophthalmol. *14*(1), 626–639.

936

937 34. Lin, S., Vermeirsch, S., Pontikos, N., Martin-Gutierrez, M.P., Daich Varela, M.,
938 Malka, S., Schiff, E., Knight, H., Wright, G., Jurkute, N., et al. (2024). Spectrum of
939 Genetic Variants in the Most Common Genes Causing Inherited Retinal Disease in a

940 Large Molecularly Characterized United Kingdom Cohort. Ophthalmol. Retina. *8*(7),
941 699–709.
942
943 35. Sai, H., Ollington, B., Rezek, F. O., Chai, N., Lane, A., Georgiadis, T., Bainbridge,
944 J., Michaelides, M., Sacristan-Reviriego, A., Perdigão, P. R. L., Leung, A., van der
945 Spuy, J. (2024). Effective AAV-mediated gene replacement therapy in retinal
946 organoids modeling AIPL1-associated LCA4. Mol. Ther. Nucleic Acids. *35*(1), 102148.
947
948 36. Zhou, T., Benda, C., Dunzinger, S., Huang, Y., Ho, J. C., Yang, J., Wang, Y.,
949 Zhang, Y., Zhuang, Q., Li, Y., et al. (2012). Generation of human induced pluripotent
950 stem cells from urine samples. Nat. Protoc. *7*(12), 2080–2089.
951
952 37. Hildebrand, L., Rossbach, B., Kühnen, P., Gossen, M., Kurtz, A., Reinke, P.,
953 Seemann, P., Stachelscheid, H. (2016). Generation of integration free induced
954 pluripotent stem cells from fibrodysplasia ossificans progressiva (FOP) patients from
955 urine samples. Stem Cell Res. *16*(1), 54–58.
956
957 FIGURE LEGENDS
958 **Figure 1. Phenotypic characterisation of isogenic and R345W iRPE**
959 (A) Bright field microscopy and IF of iRPE from ISOCON and R345W iRPE at day 60
960 of differentiation, showing pigmented cobblestone morphology, tight junction formation
961 (ZO-1, green) and pre-melanosome (PMEL, magenta) protein expression. Nuclei
962 (blue) are labelled with DAPI. Scale bars, 50 μm.
963 (B) Western blot analysis of protein extracts from ISOCON and R345W iRPE for ZO-
964 1, Ezrin and MERTK.

965 (C) IF of ISOCON and R345W iRPE at day 80 of differentiation and (D) at day 96 of
966 differentiation. Progressive disorganisation of the R345W iRPE is evident with patchy
967 PMEL17 (magenta) expression and Ezrin (green) disorganisation, and accumulation
968 of drusen-associated proteins COL4 (green) and APOE (magenta). Nuclei (blue) are
969 labelled with DAPI. Scale bars, 50 μm.
970
971 **Figure 2. Phenotypic abnormalities are exacerbated in R345W iRPE over time**
972 (A) IF of transverse sections (day 98 of differentiation) of ISOCON and R345W iRPE
973 for apical marker Ezrin (green) and basement layer marker COL4 (magenta), revealing
974 a more disorganised RPE monolayer in the R345W iRPE and remodelling of the basal
975 layer. Nuclei (blue) are labelled with DAPI. Scale bars, 25 μm.
976 (B) IF of transverse sections (day 98 of differentiation) of ISOCON and R345W iRPE
977 for PMEL (green) and ZO-1 (magenta). Both ISOCON and R345W iRPE are
978 pigmented (PMEL), but the ZO-1 staining in the R345W iRPE is irregular. Nuclei (blue)
979 are labelled with DAPI. Scale bars, 25 μm.
980 (C) IF of transverse sections (day 98 of differentiation) of ISOCON, R345W, and
981 ISOKO iRPE for F3 (green) and COL4 (magenta). IF shows disorganisation of the
982 R345W iRPE monolayer, basal accumulation of COL4 and altered organisation of F3.
983 No accumulation of COL4 and F3 is seen in the ISOKO iRPE. Nuclei (blue) are
984 labelled with DAPI. Scale bars, 25 μm.
985 (D) Upper panel: Representative TEM images showing characteristic morphology of
986 polarized pigmented RPE in ISOCON and R345W iRPE. Basal deposits are visible
987 between the basal membrane (blue outline) and the underlying transwell membrane
988 in R345W iRPE. Scale bar, 2 μm. Lower panel: Representative TEM images showing

989 altered mitochondria morphology (false-coloured green) in R345W iRPE. Scale bar,
990 500 nm.
991
992 **Figure 3. *In vitro* screen of *EFEMP1*-targeting ASO in HEK293T cells**
993 (A) *In silico* analysis of *EFEMP1* (exon 10 mRNA) (RNAstructure University of
994 Rochester). The c.1033C>T, p.Arg(345Trp) variant is highlighted by an arrow and the
995 binding of ASO1 shown. The calculated difference in free energy between the target
996 sequence alone (lowest free energy value of -21.9 kcal/mol) and the ASO1-bound
997 target sequence (-54.0 kcal/mol) is >21 kcal/mol meeting the requirements for stable
998 ASO targeting.[21]
999 (B, C, D) qPCR analysis of R345W *EFEMP1* (B), WT *EFEMP1* (C) and TOTAL
1000 *EFEMP1* (D) transcript levels following transfection of HEK293T cells with
1001 pEFEMP1(R345W)-mScarlet and pEFEMP1(WT)-3xFLAG together with control ASO
1002 (CTRL) (50 nM) or increasing amounts (25 nM, 50 nM, 100 nM, 200 nM) of ASO1,
1003 ASO2, ASO3 and ASO4. *EFEMP1* transcript levels are expressed relative to the
1004 untreated 'plasmid only' condition. No expression of *EFEMP1* was detected in cells
1005 that were treated with transfection reagent only (untransfected, UT). The experiment
1006 was repeated three times (N=3) with four technical replicates (n=4) per condition in
1007 each experiment. Bars represent mean ± SEM.
1008 (E) qPCR analysis of TOTAL (black bars), R345W (light grey bars) and WT (dark grey
1009 bars) *EFEMP1* transcript levels following the transfection of HEK293T cells with
1010 pEFEMP1(R345W)-mScarlet and pEFEMP1(WT)-3xFLAG together with control ASO
1011 (CTRL) (50 nM) or increasing amounts (25 nM, 50 nM, 100 nM, 200 nM) of ASO1.1,
1012 ASO1.2, ASO1.3 and ASO1.4. *EFEMP1* transcript levels are expressed relative to the
1013 untreated 'plasmid only' condition. The experiment was repeated three times (N=3)

1014 with four technical replicates (n=4) per condition in each experiment. Bars represent
1015 mean ± SD.
1016
1017 **Figure 4. *EFEMP1* allele-specific targeting in iRPE following ASO transfection**
1018 (A-D) iRPE were transfected with ASO1.1, 1.2, 1.3, 1.4 or control ASO (CTRL) (200
1019 nM) at day 72 of differentiation and analysed 48 hours later.
1020 (A) Fluorescence and bright field images of R345W iRPE showing efficient delivery of
1021 6-FAM conjugated ASO.
1022 (B) Quantitation of *EFEMP1* transcript levels by qPCR. All ASO mediate a significant
1023 decrease in *EFEMP1* levels. N = 3 independent experiments, n = 2 technical replicates
1024 of each condition per experiment. Statistical significance was determined by one-way
1025 ANOVA followed by post-hoc Tukey's (HSD) test where *, ** and *** denotes a *p* value
1026 <0.05, 0.01 and 0.005 respectively. ns = not significant. Bars represent mean ± SEM.
1027 (C) Sanger sequencing chromatograms of untreated (NT) R345W iRPE and R345W
1028 iRPE treated with CTRL ASO, ASO1.1, ASO1.2, ASO1.3 or ASO1.4 (200 nM). The
1029 heterozygous 'C/T' peak in the NT and CTRL treated R345W iRPE is resolved to a
1030 homozygous 'C' peak in all ASO treated samples.
1031 (D) Quantitation of ASO-mediated allele-specific *EFEMP1* targeting by NGS. WT (%C)
1032 and R345W (%T) *EFEMP1* transcript levels were quantified in untreated R345W iRPE
1033 (NT) or R345W iRPE treated with CTRL or therapeutic ASO1.1, 1.2, 1.3 or 1.4. NGS
1034 results for gDNA and cDNA from corresponding patient renal epithelial cells are also
1035 shown. N = 3 independent experiments, n = 2 technical replicates of each condition
1036 per experiment. Bars represent mean ± SD.
1037 (E) Integrated analysis of the qPCR and NGS data showing a significant reduction of
1038 the R345W transcript with all ASO. Statistical significance was determined by one-

1039 way ANOVA followed by post-hoc Tukey's (HSD) test where *, ** and *** denotes a *p*
1040 value <0.05, 0.01 and 0.005 respectively. ns = not significant. Bars represent mean ±
1041 SD.
1042
1043 **Figure 5. *EFEMP1* allele-specific targeting in iRPE following ASO gymnosis**
1044 (A-C) R345W iRPE at day 60 of differentiation underwent a 7-day treatment with
1045 control ASO (CTRL) (1 μM) or ASO1.1 at the doses 0.5 μM, 1 μM, 5 μM and 10 μM.
1046 (A) Fluorescence from gymnotically delivered 6-FAM-conjugated ASO1.1 (1 μM)
1047 showed efficient uptake predominately in the nucleus and extra-nuclear endocytic
1048 vesicles. Nuclei are labelled with DAPI. Inset shows higher magnification image. Scale
1049 bar, 50 μm.
1050 (B) Quantitation of *EFEMP1* transcript levels by qPCR. All doses of ASO1.1 mediate
1051 a significant decrease in *EFEMP1* expression levels relative to the non-treated (NT)
1052 and CTRL ASO-treated R345W iRPE. N = 2 independent experiments, n = 3 to 4
1053 technical replicates for each condition per experiment. Statistical significance was
1054 determined by one-way ANOVA followed by post-hoc Tukey's (HSD) test where *, **
1055 and *** denotes a p value <0.05, 0.01 and 0.005 respectively. Bars = mean ± SD.
1056 (C) Quantitation of ASO1.1-mediated allele-specific *EFEMP1* targeting by NGS at
1057 doses 0.5 μM, 1 μM, 5 μM and 10 μM. WT (%C) and R345W (%T) *EFEMP1* transcript
1058 levels were quantified in untreated R345W iRPE (NT) or R345W iRPE treated with
1059 CTRL or ASO1.1. N = 2 independent experiments, n = 2 technical replicates for each
1060 condition per experiment.
1061 (E) Integrated analysis of the qPCR and NGS data showing a significant reduction of
1062 the R345W transcript with all ASO1.1 doses. Statistical significance was determined

1063 by one-way ANOVA followed by post-hoc Tukey's (HSD) test where *, ** and ***
1064 denotes a p value <0.05, 0.01 and 0.005 respectively. Bars = mean ± SD.
1065
1066 **Figure 6. Phenotypic rescue of APOE and lipid accumulation in R345W iRPE**
1067 **following ASO gymnosis**
1068 (A) IF of APOE in ISOCON, ISOKO, untreated R345W (NT) and R345W iRPE treated
1069 gymnotically with ASO1.1 (1 μM dose for 7 days from day 60 of differentiation),
1070 showing APOE (magenta) accumulation in R345W iRPE and rescue in ASO1.1
1071 treated R345W iRPE. Nuclei are labelled with DAPI. Scale bars, 50 μm.
1072 (B) Quantitation of APOE (relative fluorescence levels) in ISOCON, untreated R345W
1073 iRPE (NT) and ASO1.1 treated R345W iRPE (1 μM dose for 7 days from day 60 of
1074 differentiation). Fluorescence levels were quantified from four independent images.
1075 Statistical significance was determined by one-way ANOVA followed by post-hoc
1076 Tukey's (HSD) test where *, ** and *** denotes a p value <0.05, 0.01 and 0.005
1077 respectively. Bars = mean ± SD.
1078 (C) Images of transverse sections (14 μM) from ISOCON and R345W iRPE treated
1079 gymnotically with CTRL ASO or with therapeutic ASO1.1 (1 μM and 5 μM dose for 14
1080 days from day 84 of differentiation), showing accumulation of neutral lipid (BODIPY,
1081 green) and basal APOE (magenta) accumulation in R345W iRPE that is rescued
1082 following ASO1.1 treatment. Nuclei are labelled with DAPI. Scale bars, 20 μm.
1083
1084 **Figure 7. Phenotypic rescue of APOE, ECM abnormalities and sub-RPE lipid**
1085 **deposition in R345W iRPE following ASO gymnosis**
1086 (A, B) Staining of ISOCON, untreated R345W (NT) and R345W iRPE following 2-
1087 month ASO1.1 gymnosis (1 μM) from day 100 of differentiation.

1088 (A) Accumulation of lipids (BODIPY, green) and APOE (magenta) was evident in NT
1089 R345W iRPE and was rescued following treatment with therapeutic ASO1.1. Nuclei
1090 are labelled with DAPI. Scale bars, 50 μm.
1091 (B) Accumulation of COL4 and F3 is evident in NT R345W iRPE and is rescued
1092 following treatment with therapeutic ASO1.1. Nuclei are labelled with DAPI. Scale
1093 bars, 50 μm.
1094 (C-E) Quantitation of relative fluorescence levels of BODIPY (C), APOE (D) and COL4
1095 (E). Statistical significance was determined by one-way ANOVA followed by post-hoc
1096 Tukey's (HSD) test where *, ** and *** denotes a p value <0.05, 0.01 and 0.005
1097 respectively. Bars = mean ± SD.
1098 (F) TEM of ISOCON, untreated R345W (NT) and R345W iRPE following 2-month
1099 ASO1.1 gymnosis (1 μM) from day 100 of differentiation. Upper panel: ISOCON,
1100 untreated R345W and ASO1.1 treated R345W iRPE show a characteristic RPE-like
1101 morphology. Scale bars, 2μm. Lower panel: Representative TEM images of basal
1102 deposits between the basal membrane (blue outline) and the underlying transwell
1103 membrane. Scale bars, 500 nm.
1104

1105 FIGURE 1

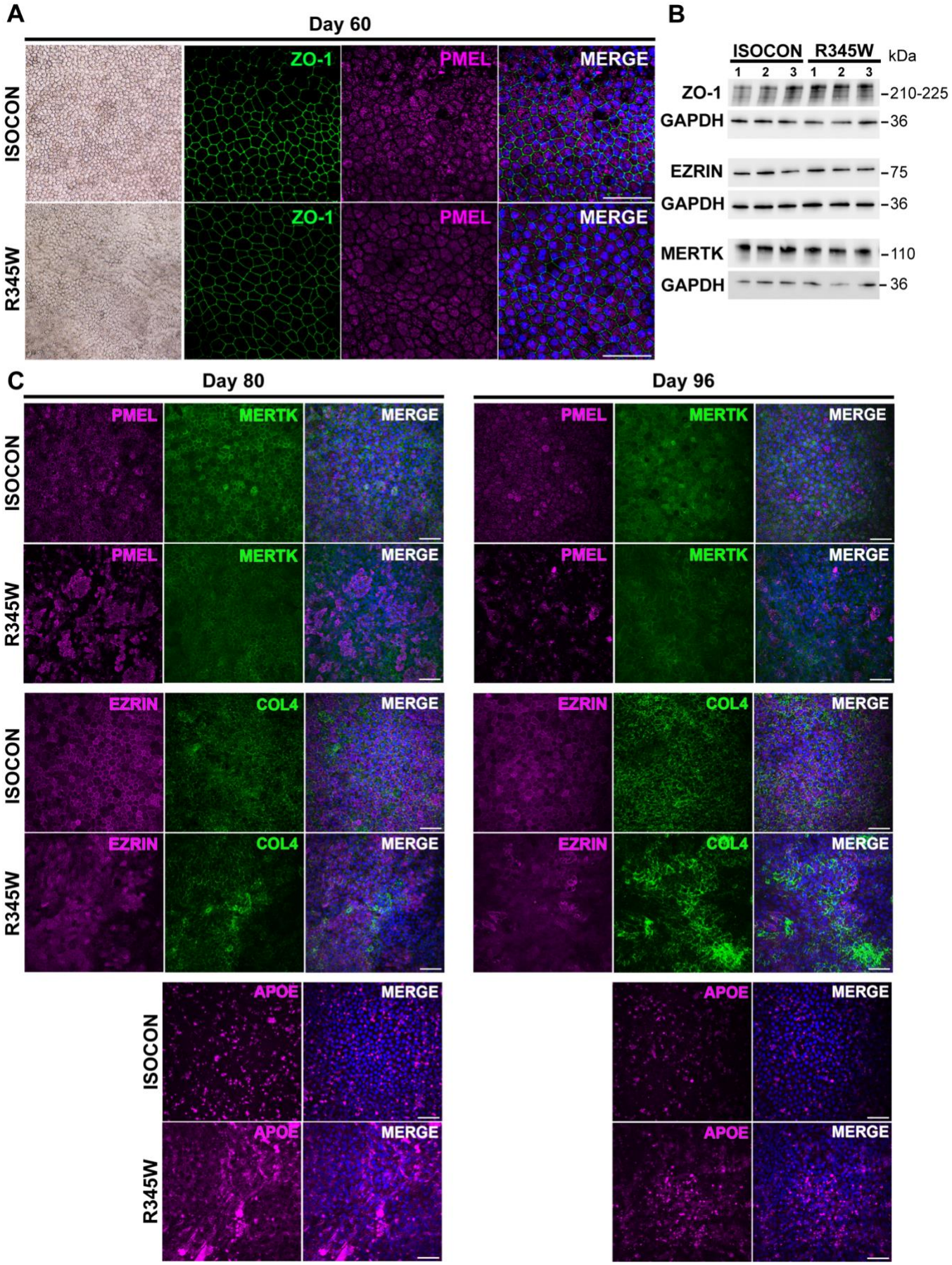

1106 FIGURE 2

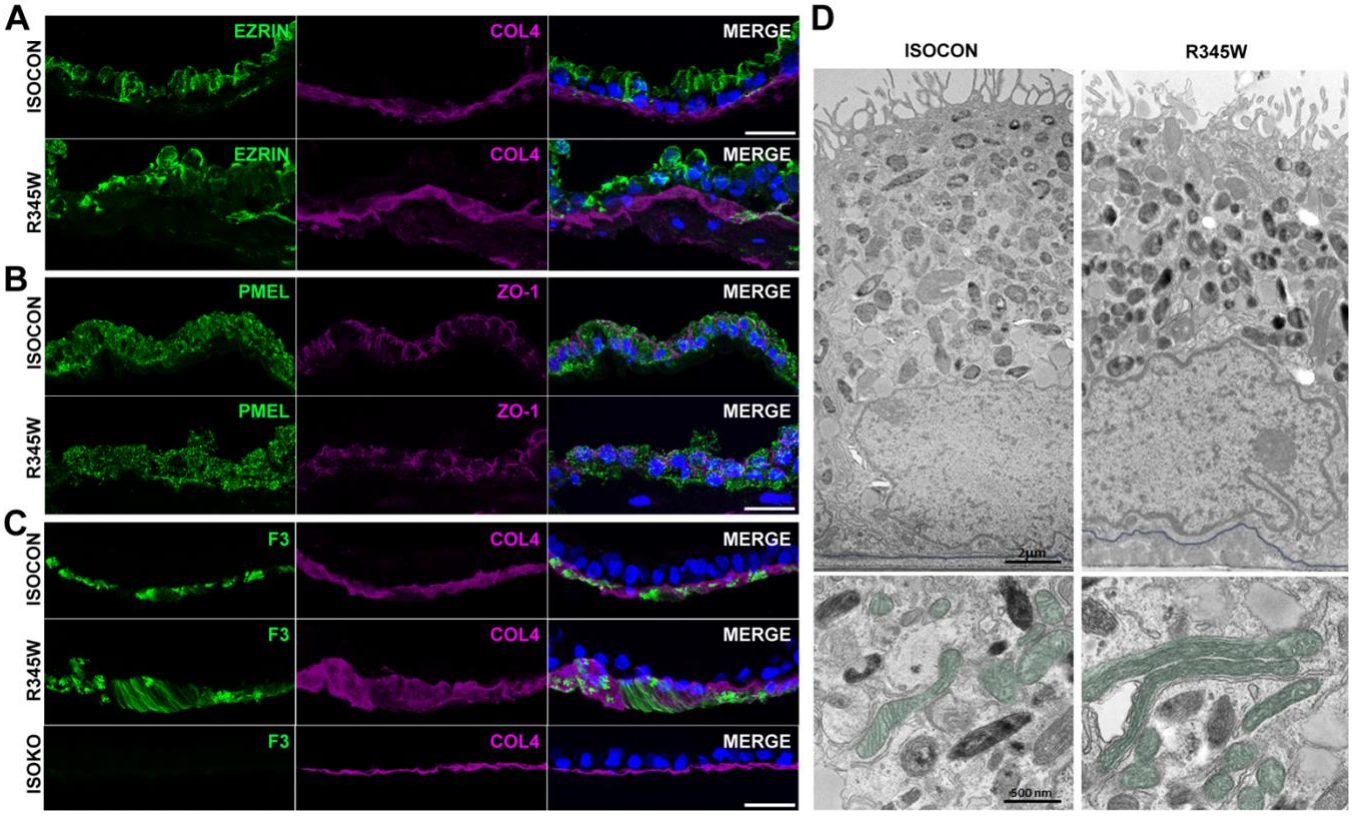

1107 FIGURE 3

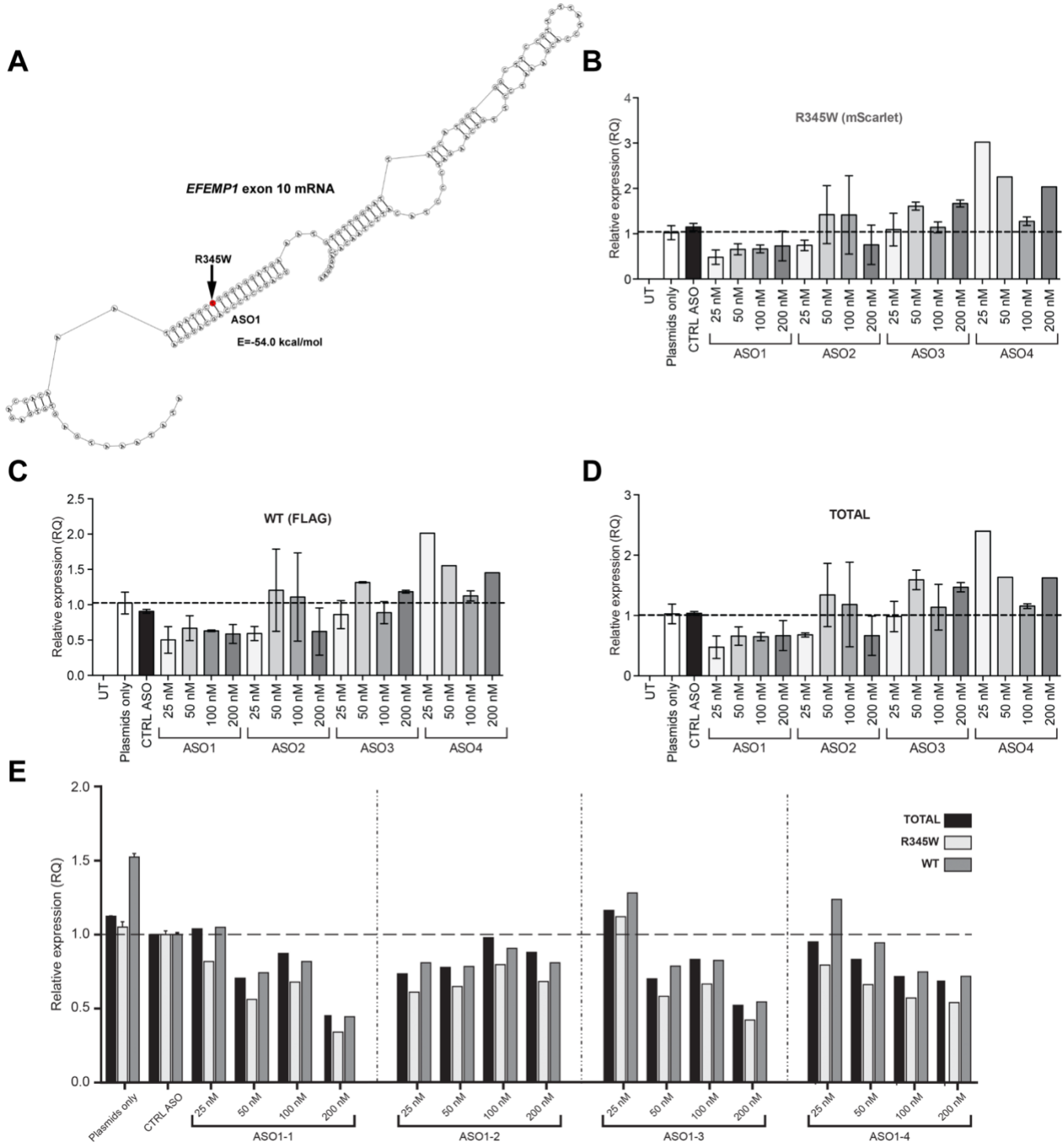

1108

1109 FI GURE 4

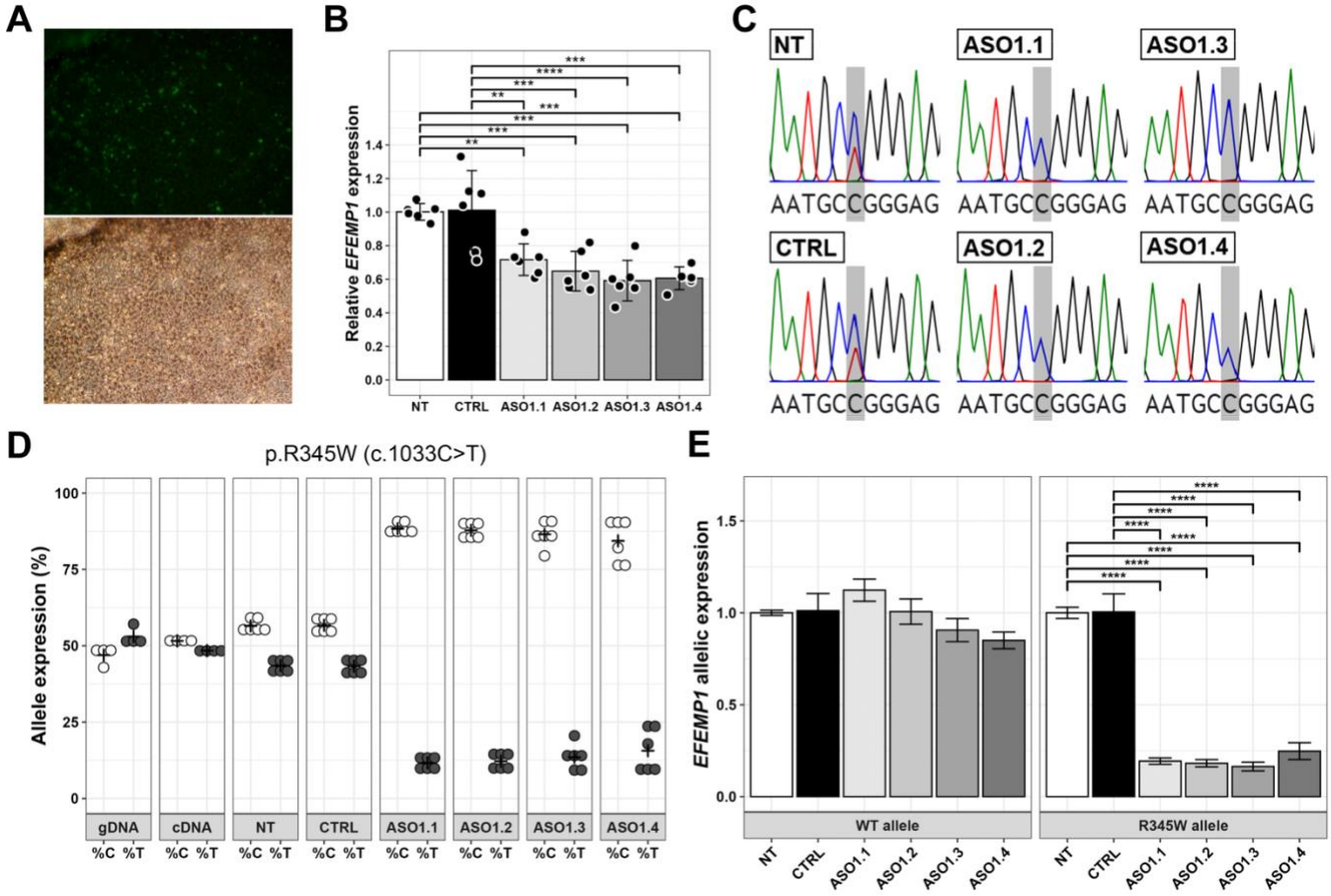

1110 FIGURE 5

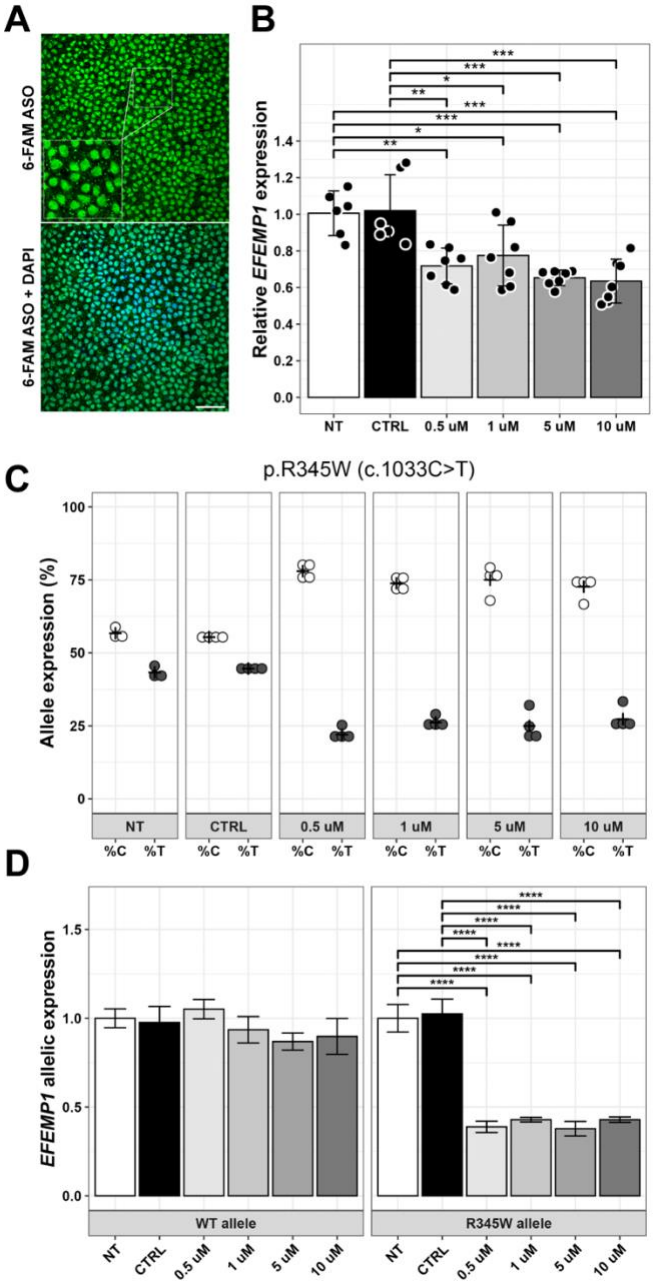

1111 FIGURE 6

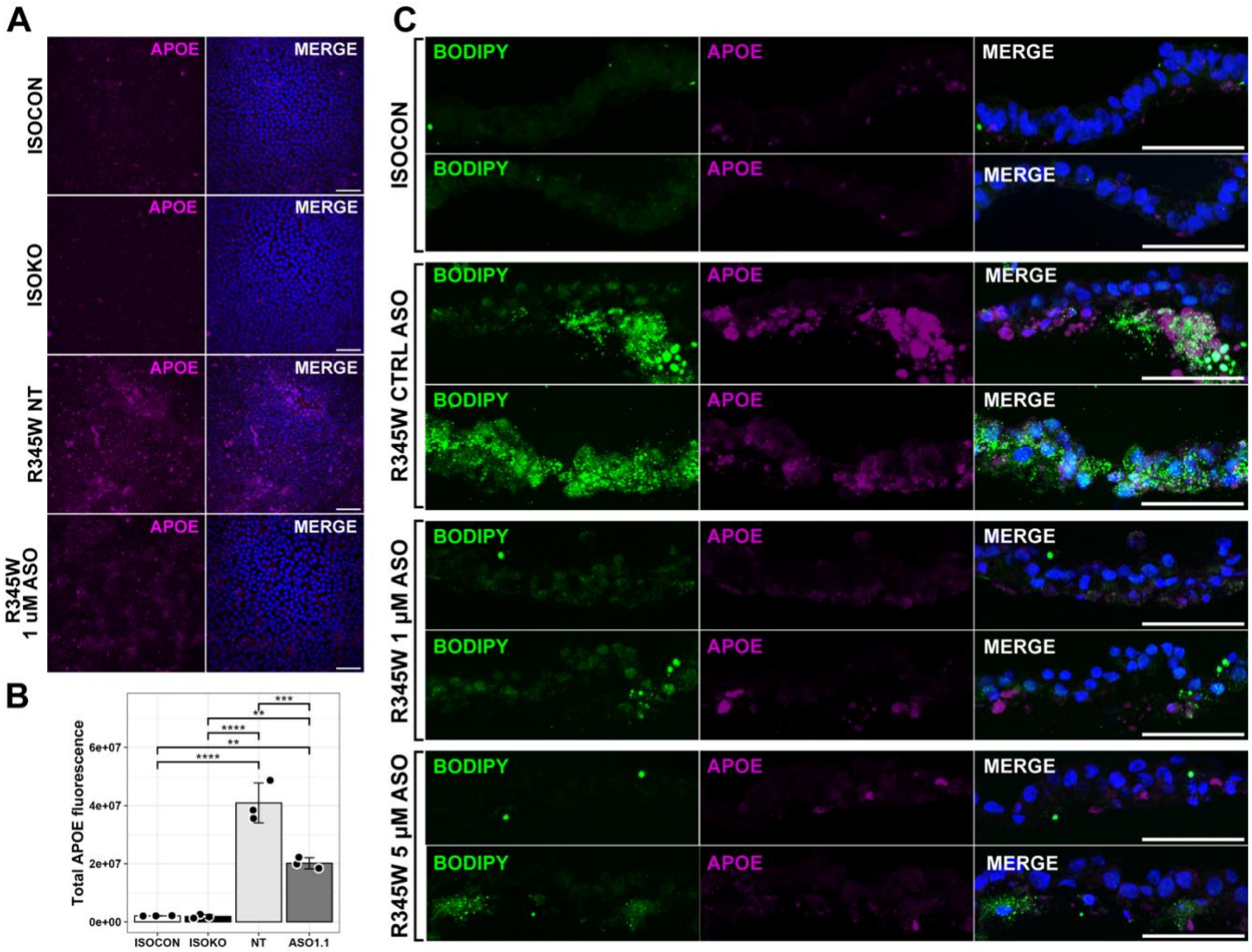
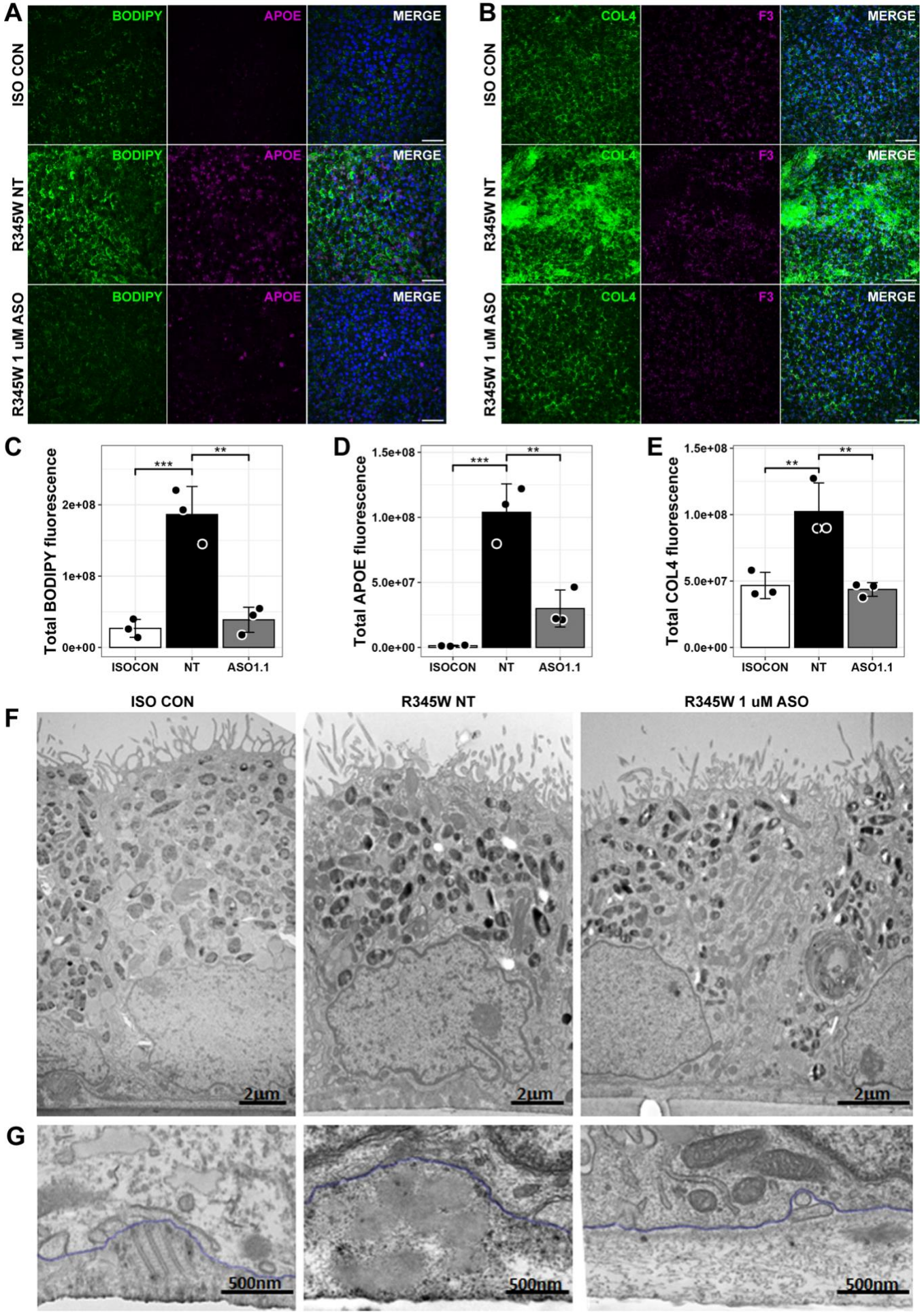
1112 FIGURE 7